HHS Public Access

Author manuscript

*Cell Rep*. Author manuscript; available in PMC 2023 June 27.

Published in final edited form as:

*Cell Rep*. 2023 May 30; 42(5): 112531. doi:10.1016/j.celrep.2023.112531.

# MYO10 regulates genome stability and cancer inflammation through mediating mitosis

**Franklin Mayca Pozo**[1,*], **Xinran Geng**[1], **Masaru Miyagi**[1], **Amanda L. Amin**[2,3], **Alex Y. Huang**[4,5,6], **Youwei Zhang**[1,7,*]

[1]Department of Pharmacology, Case Western Reserve University, School of Medicine, Cleveland, OH 44106, USA

[2]Division of Surgical Oncology, Department of Surgery, University Hospitals Cleveland Medical Center, Cleveland, OH 44106, USA

[3]Seidman Cancer Center, University Hospitals Cleveland Medical Center, Cleveland, OH 44106, USA

[4]Center for Pediatric Immunotherapy at Rainbow, Angie Fowler AYA Cancer Institute, University Hospitals, Cleveland, OH 44106, USA

[5]Division of Pediatric Hematology/Oncology, University Hospitals Rainbow Babies & Children's Hospital, Cleveland, OH 44106, USA

[6]Department of Pediatrics, Case Western Reserve University, School of Medicine, Cleveland, OH 44106, USA

[7]Lead contact

## SUMMARY

Genomic instability can promote inflammation and tumor development. Previous research revealed an unexpected layer of regulation of genomic instability by a cytoplasmic protein MYO10; however, the underlying mechanism remained unclear. Here, we report a protein stability-mediated mitotic regulation of MYO10 in controlling genome stability. We characterized a degron motif and phosphorylation residues in the degron that mediate β-TrCP1-dependent MYO10 degradation. The level of phosphorylated MYO10 protein transiently increases during mitosis, which is accompanied by a spatiotemporal cellular localization change first accumulating at the centrosome then at the midbody. Depletion of MYO10 or expression of MYO10 degron mutants, including those found in cancer patients, disrupts mitosis, increases genomic instability and inflammation, and promotes tumor growth; however, they also increase the sensitivity of



*Correspondence: fxm130@case.edu (F.M.P.), yxz169@case.edu (Y.Z.).

AUTHOR CONTRIBUTIONS

F.M.P. and Y.Z. conceived the project. F.M.P. acquired most data. X.G. assisted with data acquisition. M.M. analyzed the mass spectrometry data. A.L.A. and A.Y.H. provided conceptual assistance. F.M.P. and Y.Z. wrote the manuscript.

DECLARATION OF INTERESTS

The authors declare no competing interests.

SUPPLEMENTAL INFORMATION

Supplemental information can be found online at https://doi.org/10.1016/j.celrep.2023.112531.

cancer cells to Taxol. Our studies demonstrate a critical role of MYO10 in mitosis progression, through which it regulates genome stability, cancer growth, and cellular response to mitotic toxins.

## In brief

Mayca Pozo et al. demonstrate a protein stability-coupled spatiotemporal regulation of MYO10 during mitotic progression, which is critical for maintaining genome stability. Manipulating the MYO10 expression level leads to increased sensitivity to Taxol, revealing an anticancer strategy for cancers expressing high-level or stabilized cancer mutations of MYO10.

## Graphical Abstract

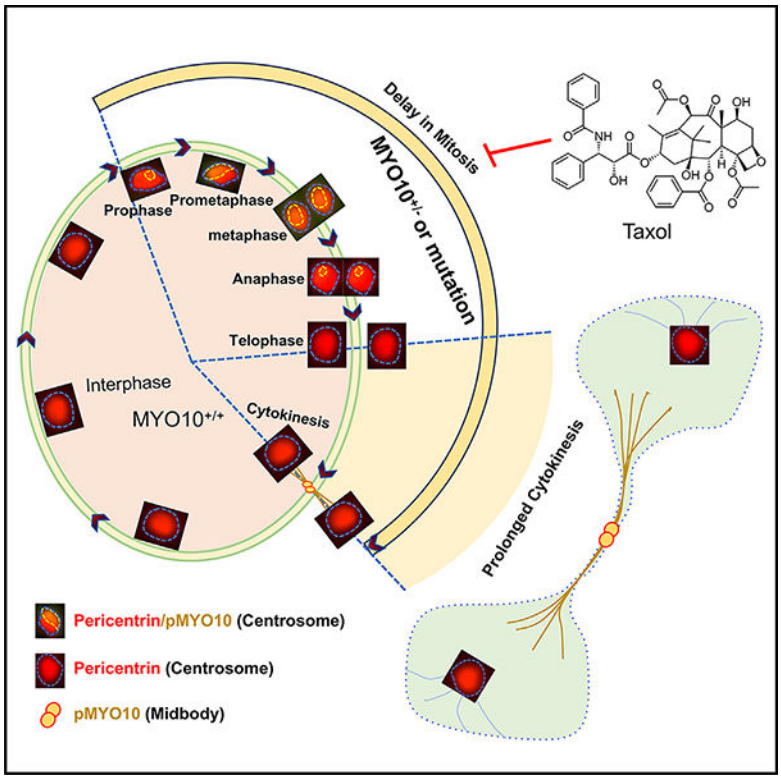


## INTRODUCTION

Scheduled mitosis is key to faithfully segregate duplicated chromosomes and therefore the maintenance of genome stability. Abnormal mitosis may lead to aneuploidy and chromosome instability (CIN), promoting cancer development.[1] Mitotic progression is typically controlled by two checkpoint events: the spindle assembly checkpoint controlling the metaphase-to-anaphase transition and the abscission checkpoint controlling the cytoplasm cleavage in cytokinesis. Whereas the spindle assembly checkpoint ensures an even attachment of condensed sister chromatids to the opposing spindle poles, the abscission checkpoint prevents unscheduled chromosome bridges between two daughter cells. These checkpoints are delicately regulated by a myriad of events, including centrosome maturation, spindle pole formation, microtubule bundle assembly, kinetochore attachment, cleavage

furrow formation, midbody assembly, etc. Abnormalities in any of these processes may lead to faulty chromosome segregation, contributing to genomic instability and tumor evolution.[2]

Centrosomes, although not essential for somatic cells in *Drosophila*,[3] are important for mitotic fidelity by controlling the spindle pole organization.[4] Centrosome abnormalities (e.g., altered number, size, or shape) can occur concurrently with CIN in human carcinoma *in situ*,[5] suggesting that centrosome defects may contribute to early cancer development.[4] Centrosomes exert at least two layers of function in mitosis: establishment of mitotic spindle poles with correct position and orientation, and activation of cell-cycle signaling, including Cyclin B1/CDK1 (cyclin-dependent kinase 1), Aurora kinase A, and PLK1 (polo-like kinase 1).[4,6–8] Cytokinesis is the final stage of the cell division cycle that cleaves the cytoplasmic membrane shared by two daughter cells, which requires a structural organelle called the midbody formed at the connecting cytoplasm that also determines the abscission point.[9]

Mitotic cells undergo drastic morphological changes, including cellular structural network re-organization and chromosome re-arrangement. These physical changes require forces provided by several proteinaceous networks formed by actins, tubulins, and myosins. The myosin family is composed of up to 79 classes of actin-binding motor proteins from more than 900 species[10] and regulates cell deformation, migration, and division.[11] Among them, myosin II is widely known for regulating mitosis and cytokinesis.[12] However, other members have also been reported to regulate mitosis, including the non-conventional myosin, MYO10.

MYO10 belongs to the class X myosin family that contains a MyTH4 (myosin tail homology 4) and an FERM (band4.1, ezrin, radixin, moesin) domain at the carboxyl terminus.[13] Although the amino terminus of MYO10 binds actin fibers and provides motor activity,[14–16] the carboxyl-terminal FERM and MyTH4 domains are engaged in binding with tubulins and integrins to regulate cellular network organization.[17–22] MYO10 regulates centrosome position through altering the actin fiber-derived force[23] or remodels the spindle position and orientation through binding to WEE1.[24] In addition, MYO10 localizes to meiotic[17] and mitotic[18,25] spindle poles, regulating the orientation and function of the spindle pole.[18,21] A recent preprint showed that centrosome localization of MYO10 prevents multipolar spindle formation and peri-centrosome matrix fragmentation.[26]

Despite these lines of findings, how exactly MYO10 regulates mitosis remained unclear, largely because of the lack of understanding about cellular localization of endogenous MYO10, especially those with functional posttranslational modifications, during different stages of mitosis. We recently reported that MYO10 undergoes ubiquitination and proteasomal degradation by the ubiquitin E2 enzyme UbcH7 and the Skp1-CUL1-F-box$^{\beta\text{-TrCP1}}$ E3 ligase.[27] We further demonstrated that the protein level of MYO10 is key to determine the extent of genomic instability and inflammation in cancer.[27] However, how exactly MYO10 regulates genomic instability remained unknown. In this study, we report detailed mechanisms underlying MYO10 degradation and reveal spatiotemporal regulation of MYO10 during mitosis, through which it regulates genome stability, tumor growth, and cellular sensitivity to agents that target mitosis.

# RESULTS

## Identification of the degron motif for MYO10 degradation

Conventionally, genomic instability has been largely viewed as a nuclear pathophysiology caused by defects in the machineries that regulate DNA replication, repair, and segregation. We recently reported that a cytoplasmic factor MYO10 regulates genome stability, through which it promotes cancer development and immunotherapy[27]; however, mechanisms underlying the genome stability regulation of MYO10 remained unknown. Given the importance of the protein level of MYO10 in this activity,[27] we decided to further characterize MYO10 degradation mechanisms. MYO10 is a multi-domain protein (Figure 1A).[28] To determine whether MYO10 degradation depends on a degron motif, a short stretch of amino acid that drives the degradation of unstable proteins, we generated a series of truncation mutants of human MYO10 tagged with GFP (Figure 1A) and examined the protein stability in the presence of a protein synthesis inhibitor, cycloheximide (CHX). We found that fragments F2 and F4 were as unstable as the MYO10 full-length (FL) (Figure 1B). CHK1, a known unstable protein,[29,30] served as a positive control for protein degradation by CHX observed in all groups (Figure 1B). To determine which fragment is involved in MYO10 degradation, we performed co-immunoprecipitation (coIP) to determine their interactions with β-TrCP1. The results show that F2, but not F4, interacted with β-TrCP1 as strongly as MYO10 FL (Figure 1C). In addition, whereas F2 and FL of MYO10 were expressed in the cytoplasm, the F4 fragment was expressed in the nucleus (Figure S1A). Further, expression of F2 increased nuclear abnormalities as done by MYO10 FL, but not F4 (Figure S1B). Combined, these lines of evidence support the idea that the F2, but not the F4, fragment is responsible for β-TrCP1 binding and MYO10 degradation.

The F2 fragment demonstrated similar protein stability as the MYO10 FL (Figure S1C), supporting the existence of a degron in this fragment. F2 contains a PEST (Pro/Glu/Ser/Thr-rich) domain that is known to regulate protein degradation.[31] Indeed, the PEST-only domain (F2′, Figure 2A) was also unstable in the presence of CHX and stabilized by a proteasome inhibitor, MG132 (Figure 2B). Further, F2′ interacted with β-TrCP1 as strongly as F2 or FL of MYO10 (Figure 2C), suggesting the presence of a degron in the PEST domain. β-TrCP1 often recognizes a $DSG(X)_{2–4}S$ consensus degron motif in its substrate.[32,33] Interestingly, MYO10 from human and mouse, but not other species, contains a $DSG/A(X)_4S$ motif in the PEST region (Figure 2A). Consistently, human MYO10 was less stable than its bovine counterpart, in which CHK1 was similarly degraded, whereas UbcH7, the E2 enzyme for both MYO10 and CHK1 degradation,[27,34,35] was unchanged (Figure S1D). When the $DSG/A(X)_4S$ motif was deleted from human MYO10, the protein was completely stable (Figure S1E). These data strongly support the $DSG(X)_4S$ motif as the degron for human MYO10 degradation.

## Phosphorylation of degron is required for MYO10 degradation

Degron phosphorylation is often required for β-TrCP1 binding and protein degradation of the substrate.[36,37] Further, TCGA analysis revealed two mutations (S1062R and L1063P) in MYO10 degron from human cancer patients, which did not harbor any co-mutations in *BTRC* (the gene encoding β-TrCP1) (Figure S2). Hence we asked whether MYO10 is

phosphorylated in the degron. Mass spectrometry confirmed that the three Ser residues ($DS_{1060}GS_{1062}LHNS_{1066}$) in human MYO10 were indeed phosphorylated (Figure S3A). To further confirm MYO10 phosphorylation and to determine its biological significance, we generated a mouse monoclonal antibody against the phosphorylated, but not non-phosphorylated, peptide covering these three residues. This antibody recognizes both GFP-MYO10 FL and F2 proteins expressed in HEK293T cells (Figure S3B, the pMYO10 blot). Further, it recognizes endogenously phosphorylated MYO10 proteins, whose levels were increased by Taxol but abolished by phosphatase treatment (Figure S3C), confirming that this antibody indeed recognizes endogenously phosphorylated MYO10.

We noticed that phosphorylated MYO10 was less stable than total GFP-MYO10 proteins (Figure S1E, compare the GFP and the pMYO10 blots in wild-type [WT] samples), supporting the importance of phosphorylation at these residues in controlling MYO10 protein stability. To further determine the involvement of each residue in MYO10 protein stability, we generated MYO10 point mutations in the degron, including the two cancer mutations. S1060A and S1062R mutants only moderately increased the protein stability of MYO10 compared with the WT; however, L1063P, and more clearly S1066A, significantly increased the protein stability (Figures 2D and 2E), indicating critical roles of these two residues in mediating MYO10 protein stability. Consistently, the proteasome inhibitor, MG132, blocked degradation of the unstable MYO10 WT and S1062R but had little effect on the already stable L1063P or S1066A mutant (Figure 2F).

As to MYO10 phosphorylation, the S1060A mutant was phosphorylated at a level similar to that of WT (Figure 2G). S1062R greatly, but not fully, reduced MYO10 phosphorylation; however, L1063P and S1066A completely abolished MYO10 phosphorylation (Figure 2G). Endogenous pMYO10 was not detected in the input probably because the levels of overexpressed proteins were so high that they shadowed the signal of endogenous pMYO10. It is tempting to speculate that although L1063P changed the three-dimensional structure of the degron to mitigate MYO10 phosphorylation, Ser1066 is most critical for MYO10 phosphorylation.

To further probe the significance of these residues in MYO10 ubiquitination and degradation, we first examined their interaction with β-TrCP1. After adjusting the protein level of Flag-β-TrCP1 from the input, a ~35%–40% reduction in the interaction between MYO10 S1060A, S1062R, or L1063P and β-TrCP1 was observed compared with MYO10 WT; the S1066A mutant had the most reduction (Figure 2G, the Flag blots in coIP and input). Consistent with the phosphorylation and coIP results, the two cancer mutants (S1062R or L1063P) and S1066A, but not S1060A, greatly reduced GFP-MYO10 ubiquitination in cells (Figure 2G, the Ub blot in the immunoprecipitation [IP]). Combined, these results generally support the importance of L1063 and S1066, and to a lesser degree S1062, in MYO10 phosphorylation, ubiquitination, and degradation.

## Stabilizing MYO10 increased genomic instability, inflammation, and tumor growth

We recently reported that cancer cells expressing a high level of MYO10 had elevated levels of genomic instability and inflammation, through which they promoted tumor growth.[27] Because degron mutations stabilized MYO10 (strongly by L1063P and S1066A

and moderately by S1062R), we asked whether these mutations would induce genomic instability and promote inflammation and tumor growth. We have generated MYO10 knockdown U2OS and MDA-MB-231 cell lines that express a significantly reduced level of endogenous MYO10 through depleting the majority of *MYO10* alleles by CRISPR[27]; however, for easy nomenclature, we called them MYO10$^{+/-}$ cells (but in fact the protein level was reduced much more than 50%). We then stably expressed GFP-MYO10 FL/WT or mutants in these cells (Figures 3A and S3D) and chose lines expressing GFP-MYO10 proteins at comparable levels to endogenous MYO10 for further analysis. We found that re-expression of MYO10, especially the most stable S1066A mutant, elevated the levels of factors associated with inflammation, such as IL-8 and pSTAT1, in MDA-MB-231 MYO10$^{+/-}$ cells (Figures 3A, S4A, and S4B), consistent with the idea that increasing the protein level of MYO10 elevated the inflammatory response in cancer cells. MDA-MB-231 MYO10$^{+/-}$ cells proliferated slower than parental cells (Figure 3B), similar to U2OS MYO10$^{+/-}$ cells[27] and other cell lines with MYO10 depleted or inhibited.[25,38] However, overexpressing MYO10 WT or degron mutants rescued cell proliferation (Figure 3B), supporting the positive role of MYO10 in cell proliferation and indicating that phosphor-deficient mutants can also support cell growth under unstressed conditions. In contrast, depletion of β-TrCP1 slowed cell proliferation (Figure S4C), which did not phenocopy the expression of MYO10 mutant. This likely reflects the fact that β-TrCP1 has a much broader role than MYO10 in cell growth because of its regulation of a myriad of substrates.[36,37]

Next, we determined genomic instability in these clones by assessing the frequency of cells with abnormal nuclear shape, which is inversely correlated with the nuclear circularity, and micronuclei. For MDA-MB-231 parental (MYO10$^{+/+}$) cells that already have a high basal level of genomic instability, knockdown of MYO10 significantly reduced genomic instability as shown by improved nuclear shape and reduced micronuclei (Figures 3C–3E), suggesting that they are addictive to a high level of MYO10. However, re-expressing MYO10 WT or degron mutants generally restored or even enhanced the level of genomic instability (Figures 3C–3E), further supporting the idea that the protein level of MYO10 determines the extent of genomic instability in cancer cells.

The cellular level of cGAMP ($2^0 3^0$-cyclic GMP-AMP), the key molecule that activates the STING-dependent inflammation,[39] was restored in MYO10$^{+/-}$ cells expressing these clones, which is consistent with the increase in micronuclei (Figure 3F), an important source for activating the cGAS (cyclic GMP-AMP synthas)/STING pathway.[39] To determine how protein stability of MYO10 affects tumor growth, we inoculated these MDA-MB-231 cell lines into nude mice and examined tumor growth. Similar to our previous observations from other breast cancer models,[27] knockdown of MYO10 significantly reduced the growth of MDA-MB-231 tumors (Figures 3G and 3H). Re-expressing MYO10 WT, and to a higher degree the stable L1063P or S1066A mutant, resulted in further increase in tumor growth compared with parental cells (Figures 3G and 3H). The S1062R mutant did not enhance tumor growth to the level as done by the WT or other two degron mutants (Figures 3G and 3H), probably because of its weak effect on stabilizing MYO10 (Figure 2F) and inducing genomic instability (Figures 3C–3E); however, S1062R mutant tumors still grew significantly larger than MYO10$^{+/-}$ tumors (Figure 3H), reinforcing the idea that increasing the expression level of MYO10 favors tumor growth.

A review of the literature suggests that the role of the E3 ligase β-TrCP1 in tumorigenesis is less clear and somewhat contradictory. β-TrCP1 knockout mice developed normally with only minor defects in spermatogenesis,[40] suggesting that loss of β-TrCP1 does not promote tumorigenesis. Overexpression of β-TrCP1 led to increases in cell proliferation and tumor development in mammary, ovarian, uterine,[41] colon,[42] and lung,[43] suggesting a tumor-promoting role of β-TrCP1. However, it was also reported that F box deleted β-TrCP1 (dominant-negative mutant of the protein) transgenic mice developed tumors,[44] suggesting a potential tumor suppressing effect of β-TrCP1. In contrast, the role of MYO10 in tumor progression is constant with overexpression of MYO10 (WT or degron mutants) increasing tumor growth, whereas depletion of MYO10 reduces it. Again, this is likely due to the broad range of biological function of β-TrCP1, which might be dominated by non-MYO10 pathways in tumorigenesis.

To determine whether tumors expressing MYO10-stabilizing mutants indeed had elevated levels of inflammation, we measured the production of interferons and interleukins in these mouse tumors by qPCR. The results show that although knockdown of MYO10 reduced inflammatory factors in mouse tumors, re-expressing MYO10 WT or degradation defective mutants restored or even further elevated their levels (Figures S4D–S4F).

To further test the idea that MYO10 protein level positively correlates with genomic instability, we examined the impact of MYO10 knockdown or overexpression in a non-transformed cell line, ARPE-19. Whereas shMYO10 significantly reduced the protein level of MYO10, overexpression of GFP-MYO10 WT or mutants caused roughly 10%–40% increases in the protein level compared with endogenous MYO10 (Figure S5A). GFP-MYO10 WT and S1062R-expressing cells showed higher levels of pMYO10 than parental cells, which is likely the result of a combination of both endogenous and exogenous pMYO10 proteins. In contrast, cells expressing L1063P or S1066A had the same level of pMYO10 as parental cells (Figure S5A), indicating that these two mutants are not phosphorylated in ARPE-19 cells and supporting our conclusion that L1063 and S1066 residues are key for MYO10 phosphorylation. Then, we measured genomic instability of these ARPE-19 cell lines by examining the nuclear shape and the presence of micronuclei. Parental cells have a low basal level of genomic instability. Depletion of MYO10 significantly increased the levels of abnormal nuclei and micronuclei, whereas overexpressing MYO10 WT or mutants induced an even greater increase in genomic instability (Figures S5B and S5C). These findings are similar to observations from transformed U2OS cells. Our results are in line with findings from certain precancerous conditions, such as during trans-differentiation from normal esophageal squamous epithelium to Barrett's esophagus tumors, where a significant increase in *MYO10* mRNA levels was observed (Figure S5D).[45] These results support the idea that increasing the expression level of MYO10 may promote cellular transformation and cancer progression.

We noticed minor inconsistences when measuring the protein stability, phosphorylation, β-TrCP1 binding, ubiquitination, and tumor promotion for the S1062R mutant. In addition to the variable sensitivities of different assays/methods used, we observed a generally weak tumor promoting role for this mutant in both transformed and non-transformed cell lines, suggesting that S1062 is less important than L1063 or S1066 in driving MYO10 protein

stability and cellular function. In all, these results support an idea that overexpressing or stabilizing MYO10 increases genomic instability, induces inflammation, and promotes tumor growth. Due to the less stable effect of the S1062R mutation, we will focus on L1063P and S1066A mutants for subsequent studies unless specified.

## MYO10 mediates mitosis progression

MYO10 was best known for its localization at filopodia. We confirmed the filopodia localization for total proteins of GFP-MYO10 WT and degron mutants (Figure S6). Interestingly, phosphor-MYO10 was detected at filopodia for only GFP-MYO10 WT, S1060A, and S1062R, but not for L1063P or S1066A (the pMYO10 signal in L1063P- or S1066A-expressing cells was likely non-specific, because this antibody did not detect endogenous proteins in MYO10$^{+/-}$ cells as discussed later), consistent with the loss of phosphorylation by the L1063P or S1066A mutant. These data also suggest that degron motif phosphorylation is not required for filopodia localization, indicating separate function of degron phosphorylation and filopodia location of MYO10. However, the filopodia signal for endogenous MYO10 was hardly detected in our hands using different antibodies, similar to a previous report of prostate cancer cells expressing a relatively low level of MYO10[46]; instead, endogenous MYO10 was readily detected at the peri-nuclear region in interphase cells,[27] which was confirmed by overexpressed proteins (Figure S6, the GFP channel).

The peri-nuclear region is an important cellular compartment that is tightly associated with mitosis progression through regulating the reorganization of structural networks critical for mitosis, such as microtubules and the nuclear envelope. We already showed that MYO10$^{+/-}$ U2OS cells progressed through mitosis slower than parental cells,[27] and several studies have shown the location of MYO10 in mitotic or meiotic spindle poles; hence we decided to examine the detailed expression and location of MYO10 proteins, especially phosphorylated MYO10, in mitotic cells. We first observed that the level of phosphorylated MYO10 started to increase when cells enter mitosis, maintained an ~30%–70% increase during mitosis, and then declined to basal levels when cells exit mitosis, as indicated by Ser10 phosphorylated histone H3 in both A549 (Figure 4A) and U2OS cells (Figure S7A).

Second, we revealed a dynamic cellular localization of MYO10 during mitosis. Endogenous pMYO10 was detected at the centrosome starting from prophase (Figure 4B) and colocalized with centrosome markers such as γ-Tubulin and Pericentrin (Figures S8A and S8B). The signal was largely abolished in MYO10$^{+/-}$ cells (Figures S8A and S8B), confirming the staining specificity and centrosome localization of pMYO10. The size of the pMYO10-coated centrosome region is smaller than that indicated by Pericentrin (Figure S7B), indicating that pMYO10 may locate at the inner centrosome. Further, the size of the pMYO10-coated centrosome in parental cells increased from prophase to anaphase A, then rapidly declined at anaphase B (Figures 4B and S7C), a trend of change that was also revealed by Pericentrin staining in parental cells (Figure 4C). However, knockdown of MYO10 abolished the increase in centrosome size, which was rescued by GFP-MYO10 WT, as well as the stabilizing degron mutants (Figure 4C). Given that this is also the stage when pMYO10 levels increased the most (e.g., Figure 4A), these data suggest that maintaining an elevated level of pMYO10 is important for the assembly and maturation of physiological

size of centrosome from prometaphase to metaphase, which does not seem to involve degron phosphorylation per se. Yet, we noticed that L1063P and S1066A, but not S1062R, displayed an even larger increase in centrosome size than WT measured by endogenous Pericentrin (Figures 4C and S9), indicating that MYO10 degron mutants over-rescued the centrosome defect, correlating with mitotic abnormalities that will be discussed later. These data further support our conclusion that the S1062 residue contributes very weakly to the function of MYO10.

Subsequently, pMYO10 starts to enrich at the central spindle microtubules during telophase and then at the intercellular bridge flanking the midbody in cytokinesis (Figure 4B). The same spatiotemporal changes were observed for total MYO10 proteins (Figure S10A), although the signal at centrosome was somewhere different: although the signal for MYO10 was generally dull and did not form a sharp bright dot, that of pMYO10 was sharp and concentrated on centrosome, indicating possibly substructural differences between total and phosphorylated MYO10 at the centrosome, which needs further investigation. Nonetheless, the signals were confirmed by knockdown of MYO10 (Figure S10B). Centrosome and spindle pole localization of MYO10 has been reported for *Xenopus laevis* embryos and egg extracts[18,24] and glioblastoma cells.[25] However, the central spindle and midbody localization and the spatiotemporal change of MYO10/pMYO10 in mitosis have not been previously reported. These results support dual roles of MYO10 in regulating two critical steps in mitosis: (1) centrosome maturation before metaphase, and (2) intercellular bridge abscission during cytokinesis.

To test this idea, we synchronized U2OS parental, MYO10$^{+/-}$, and MYO10$^{+/-}$ cells stably expressing GFP-MYO10 WT or degron mutants at the G1/S boundary by double-thymidine block and release, collected cells after 8–15 h of release, and analyzed detailed mitosis progression. Based on the DNA pattern indicated by DAPI (4′,6-diamidino-2-phenylindole) staining, we categorized cells into five sequential mitotic stages: M1–M5 (Figure S11A). By counting the percentage of cells at each of these five stages during each time point, we determined a dynamic mitotic progression profile at single-cell levels. The results show that at 8-h release, nearly 50% of parental and MYO10$^{+/-}$ cells expressing GFP-MYO10 WT, L1063P, or S1066A entered the prometaphase stage; however, MYO10$^{+/-}$ cells have not entered mitosis yet (Figure S11B). At 10 h post-release and onward, whereas parental and MYO10$^{+/-}$ cells expressing GFP-MYO10 WT or degron mutants moved through the metaphase-anaphase transition at a comparable pace, MYO10$^{+/-}$ cells were clearly arrested there (Figures S11C–S11E, accumulation of M2 in MYO10$^{+/-}$ cells). These results are consistent with the delayed metaphase progression in *Xenopus laevis* embryo treated with Myo10 morpholino oligos[18] or *PTEN*$^{-/-}$ glioblastoma cells with MYO10 depletion.[25] In the meantime, cells expressing the L1063P or S1066A mutant were accumulated in cytokinesis (Figure S11E, the M5 population), indicating a defect in the completion of cytokinesis by these mutants. Together, these data suggest that MYO10 promotes the metaphase progression and the completion of cytokinesis, supporting an important role of pMYO10 and MYO10 in mitosis progression.

### MYO10 mutants with mitotic defects increased genomic instability

We noticed that although MYO10$^{+/-}$ cells progressed through the metaphase-anaphase transition slower, those expressing the L1063P or S1066A mutant stayed longer in cytokinesis (Figure S11E). These results indicate that reducing or increasing too much of the protein level of MYO10 causes similar abnormal mitotic progression, a consequence of which would be genomic instability. To test this idea, we assessed the ratio of chromosomal abnormalities indicated by DAPI at different stages of mitosis (Figure 5A) in cells expressing a reduced level or stabilized form of MYO10. Because overexpressing MYO10 in cell lines that already have a high level of genomic instability, such as MDA-MB-231, only marginally further increased genomic instability[27] (Figures 3C–3E), we used U2OS, a cell line that has relatively low basal level of mitotic abnormalities (<5%; Figure 5B), for better evaluation.

The results show that knockdown of MYO10 greatly increased mitotic abnormalities compared with parental cells (Figure 5B). Re-expressing GFP-MYO10 WT reduced the increased mitotic abnormality in MYO10$^{+/-}$ cells, although it was slightly higher than that in parental cells, which is consistent with our previous observation that overexpressing even MYO10 WT increased genomic instability in U2OS cells.[27] In contrast, MYO10$^{+/-}$ cells expressing degradation-defective mutants (L1063P or S1066A) displayed even higher levels of mitotic abnormalities than MYO10$^{+/-}$ cells, especially during telophase/cytokinesis (Figure 5B).

We then further assessed the completion of cytokinesis by α-Tubulin staining. We observed a significant increase in the percentage of MYO10$^{+/-}$ cells with intercellular bridges even when two daughter cells have migrated far away from each other (Figures 5C and 5D). Re-expression of GFP-MYO10 WT rescued the intercellular bridge level to the one seen in U2OS parental cells; however, cells expressing MYO10 degron mutants retained higher levels of intercellular bridges than WT cells, although lower than (but not statistically different from) MYO10$^{+/-}$ cells (Figures 5C and 5D). Given that MYO10 and pMYO10 levels temporarily rise during mitosis and return to normal after mitotic exit, and they both locate at the midbody, these results suggest that MYO10 facilitates the completion of cytokinesis. Hence both significant reduction and stabilization in the level of MYO10 resulted in similar defects or delays in cytokinesis. Together with the centrosome size results, these data support a multifunctional role of MYO10 in mitosis: centrosome maturation and the completion of cytokinesis.

Prolonged existence of intercellular bridge may give rise to bi/poly-nuclei cells.[47,48] Because we observed an increase in intercellular bridges in MYO10$^{+/-}$ and MYO10$^{+/-}$ cells expressing MYO10 degron mutants, we asked whether these cells would form tetraploidy. Under normal growth conditions, the appearance of bi/poly-nuclei in U2OS cells was rare even for MYO10$^{+/-}$ cells, probably because once such cells were produced, they were immediately cleared or eliminated during the subsequent cell cycle by cell death mechanisms. Similarly, HeLa cells depleted of MYO10 by small interfering RNA (siRNA) did not show elevated basal level of binuclei.[21] Hence, to facilitate the observation of bi/poly-nuclei cells, we treated cells with cytochalasin D, an agent blocking the completion of cytokinesis through disrupting actin polymerization.[49,50]

The results show that about 10% of parental U2OS cells formed bi/poly-nuclei in the presence of cytochalasin D (Figures 6A and 6B). The ratio of bi/poly-nuclei cells was doubled when MYO10 was knocked down, which was rescued by re-expressing GFP-MYO10 WT, but not the degradation-defective MYO10 mutants (Figures 6A and 6B). In addition, other forms of cytokinesis failure, such as the formation of micronuclei,[51] were observed in cells with MYO10 greatly reduced or stabilized (Figure 3E). These results further support the idea that degradation-defective MYO10 mutants failed to support the completion of cytokinesis.

### MYO10 protein stability influences cancer cell response to mitotic toxins

Given the role of MYO10 in mitotic fidelity, we asked whether it regulates the sensitivity of cells to mitotic toxins. Indeed, MYO10$^{+/-}$ U2OS cells were more sensitive to Taxol, an agent known to induce multipolar spindle and CIN,[52] than parental cells (Figure 7A). Similarly, RNA interference-mediated knockdown of MYO10 increased the sensitivity of A549 cells to Taxol (Figure S12A). In agreement with the reduced cell survival, we observed a higher increase in the cleavage of poly(ADP-ribose) polymerase (PARP), a known marker indicating apoptosis-mediated cell death,[53] in MYO10$^{+/-}$ MDA-MB-231 cells than in parental cells, particularly after Taxol treatment (Figure 7B), suggesting that loss of MYO10 leads to increased cell death. Consistently, MYO10$^{+/-}$ cells, as well as those expressing degron mutants, were more sensitive to PARP inhibitors than parental cells or MYO10$^{+/-}$ cells expressing MYO10 WT (Figure S12B).

Mitotic cell death often takes place through a process called mitotic catastrophe, in which chromosomes are highly fragmented.[54,55] We found that U2OS MYO10$^{+/-}$ cells displayed significantly increased levels of chromosome fragmentation than parental cells in the presence of Taxol (Figures 7C and 7D), which is consistent with the cell survival and PARP cleavage results. To further determine the role of MYO10 in Taxol sensitivity, we measured mitotic cell death in U2OS parental, MYO10$^{+/-}$, and MYO10$^{+/-}$ cells stably expressing MYO10 WT or degron mutants after Taxol treatment. The results show that although GFP-MYO10 WT rescued cell death of MYO10$^{+/-}$ cells, MYO10 degron mutants did not (Figure 7E), indicating that the degron mutants are defective in rescuing mitotic death by Taxol. These results suggest that greatly reducing or stabilizing MYO10 sensitizes cancer cells to agents disrupting mitotic chromosome segregation, supporting the idea that a “sweet spot or window” exists for the MYO10 protein level in regulating mitosis and genome stability.

## DISCUSSION

Genomic instability is an enabling hallmark of human cancer that can promote the occurrence of other hallmarks, leading to tumor heterogeneity and disease development.[56,57] Previously, defects in nuclear DNA metabolism such as faulty DNA repair have been mainly considered as the cause of genomic instability. However, an emerging theme is that cytoplasmic factors also regulate genome stability through less well-understood mechanisms. We recently reported that a cytoplasmic factor, MYO10, regulates genome stability and inflammation, through which it promotes cancer progression.[27] However, how

exactly MYO10 regulates genome stability remained unknown. In the current study, we report that MYO10 regulates genome stability through mediating multiple steps of mitotic progression (Figure S12C). Importantly, our findings reveal a biphasic effect of MYO10 on mitosis and genomic instability, which is similar to genes involved in mitosis, such as Aurora kinases,[58] showing the so-called Goldilocks principle in which too little or too much expression produces the same outcome.

It has been reported that depletion of MYO10[18,59] or overexpressing the microtubule-binding domain of MYO10[59] caused abnormal mitosis; however, the underlying mechanisms remained poorly understood. Here, using a newly established mouse monoclonal antibody that recognizes degron phosphorylated MYO10, we illustrate a spatiotemporal regulation of endogenous MYO10/pMYO10 during mitosis. Our data suggest a dual role of MYO10/pMYO10 in two critical steps of mitotic progression: the prometaphase-to-metaphase transition through mediating centrosome size maturation and the completion of cytokinesis through mediating the abscission. MYO10 mutants that disrupt its phosphorylation and protein stability lead to faulty mitosis and cytokinesis, supporting an important role of MYO10 in mitosis transition (Figure S12C). These data shed significant light on our understanding of the genome stability regulation by MYO10, representing conceptual advances from the previous observation of MYO10 in genome stability and cancer.

Although both depletion and overexpression of MYO10 caused similar mitotic defects, there are slight differences between these two scenarios. MYO10-depleted cells showed alterations throughout the mitosis, including smaller centrosome size, delayed prometaphase to metaphase progression, and slowed entry into and prolonged duration of cytokinesis; in contrast, cells overexpressing MYO10 degron mutants had less effect during mitosis despite slightly larger centrosome size, but with prolonged cytokinesis. The phosphorylation-defective L1063P or S1066A mutant rescued centrosome size in $MYO10^{+/-}$ cells, suggesting that MYO10 phosphorylation per se is not essential for centrosome assembly. However, these mutants failed to complete cytokinesis on time, as caused by loss of MYO10, indicating an important role of MYO10 and degron phosphorylation in the completion of cytokinesis. This is probably why under normal situations, the increased levels in pMYO10 and MTO10 in mitosis are moderate (30%–70%), and such an increase must be reverted when cells exit mitosis. Importantly, re-expressing MYO10 WT largely rescued mitotic abnormalities and genomic instability, supporting the role of mitosis regulation by MYO10 in genomic instability induction.

Mitotic abnormalities may culminate into CIN, the prevalent type of genomic instability commonly found in solid tumors.[60] Although low to intermediate levels of CIN promote tumor progression and increase tumor heterogeneity,[61] a high level of CIN can actually lead to cancer cell death[61,62] because it may disrupt the expression of genes important for cell fitness. In cancer cells expressing degradation-defective MYO10 mutants, the ratio of CIN was significantly increased, making them intolerable to additional increases in genomic instability caused by agents targeting mitosis. Hence these cancer cells are much more sensitive to mitotic toxins than parental cells, demonstrating a vulnerability of this kind of tumor.

### Limitations of the study

Although these results identify a critical role of MYO10 and its phosphorylation in mitotic progression, detailed mechanisms underlying the centrosome size maturation and the midbody cleavage by MYO10, as well as the kinase(s) phosphorylating MYO10, remain to be fully determined. MYO10 was reported to bind to the spindle pole factor TPX2,[18] which could facilitate centrosome maturation. As to cytokinesis, MYO10 might be directly involved in the actomyosin network around the cleavage furrow to rip the bridge apart,[63] which functions as an alternative mechanism to the cytoplasmatic nuclease TREX1 to resolve the linkage.[64] Alternatively, MYO10 may associate with factors that are important for the progression of cytokinesis, such as ADD1.[65] These questions warrant future independent investigation by, for instance, identifying proteins specifically bound to MYO10 in mitosis. Nonetheless, our studies reveal a detailed spatiotemporal regulation of MYO10 and pMYO10 during mitosis, supporting an important role of this factor in mitosis progression and therefore genomic instability regulation. Further, our findings suggest a strategy in treating cancers expressing high-level or degradation-defective mutants of MYO10 by pharmacologic agents that disrupt mitosis to cause significantly elevated levels of genomic instability.

## STAR⋆METHODS

### RESOURCE AVAILABILITY

**Lead contact—**Further information and request for resources and reagents should be directed and will be fulfilled by the lead contact, Dr. Youwei Zhang (yxz169@case.edu).

**Materials availability—**The unique reagents generated in this study are available from the lead contact upon request.

**Data and code availability—**All data reported in this paper will be shared by the lead contact upon request.

This paper does not report original code.

Any additional information required to reanalyze the data reported in this paper is available from the lead contact upon request.

### EXPERIMENTAL MODEL AND SUBJECT DETAILS

Human osteosarcoma U2OS (RRID: CVCL_0042), breast cancer MDA-MB-231 (RRID: CVCL_0062), lung adenocarcinoma A549 (RRID: CVCL_0023), human retinal pigment epithelium ARPE-19 (RRID: CVCL_0145), and human embryonic kidney HEK293T (RRID: CVCL_0063) cell lines were maintained in Dulbecco's modified Eagle's medium (DMEM) (#MT10013CV, Thermo Fisher/Corning, Corning, NY, USA) with 10% fetal bovine serum (FBS) (#MT35015CV, Thermo Fisher/Corning), 1% Penicillin-Streptomycin (#15140148, Cytiva/Hyclone, Logan, UT, USA), and *Mycoplasma* removing agent Plasmocin (#ant-mpt, InvivoGen, San Diego, CA, USA) in a humidified atmosphere with 5% $CO_2$ at 37°C. During experiments, antibiotics and Plasmocin were omitted. Cells

were routinely authenticated by STR profiling. Cell transfection was performed with polyethylenimine (PEI) 300 or the X-tremeGENE HP transfection reagent (Millipore/Sigma, St. Louis, MO, USA) according to the manufacture's protocols.

MYO10 knockout U2OS or MDA-MB-2312 cells were previously described,[27] which were used to stably re-express GFP-MYO10 constructs (wild type or mutants) using GFP-MYO10 vectors described below. Briefly, MYO10 knockout cells were seeded in a 6-well plate in 2 mL DMEM containing 10% FBS without antibiotic overnight, transfected with 2 μg of GFP-MYO10 (wild type or mutants) plasmids for 48 h, re-plated into 100 mm culture dishes for 24 h, added 400–600 μg/mL G418, and cultured for 7–10 days to allow the formation of surviving colonies, which were screened for expression of GFP-MYO10 proteins by Western blotting.

## METHOD DETAILS

**MYO10 plasmid construction—**The cDNAs encoding different fragments of human MYO10 (Uniprot #Q9HD67) were amplified by PCR using pEGFPC1-MYO10[27] as the template and were re-cloned into pEGFPC1 to allow the CMV promoter-driven expression of N-terminally GFP-tagged MYO10 fusion proteins: F1-GFP-MYO10 (1–850 residues), F2-GFP-MYO10 (810–1169 residues), F3-GFP -MYO10 (1169–1510 residues), F4-GFP-MYO10 (1510–1698 residues), F5-GFP-MYO10 (1698–2052 residues), and F2′-GFP-MYO10 (973–1169 residues), which were cloned into the EcoRI or KpnI and BamHI sites of the pEGFP-C1 plasmid. The primers used for PCR amplification are listed in Table S1.

Mutagenesis was performed as previously described[67] using the QuikChange site-directed mutagenesis kit (#200522) from Agilent technologies (Santa Clara, CA, USA) according to the manufacturer's protocol. MYO10 mutants carrying missense mutations (S1060A, S1062R, L1063P, and S1066A) were constructed in the full-length pEGFP/GFP-MYO10 construct, which was used to generate Degron deleted GFP-MYO10. Primers are reported in Table S1. All constructs were verified by sequencing. Flag-β-TrCP1 was previously reported.[27]

**Cell synchronization—**Cell synchronization was conducted as previously described with modifications.[68] Briefly, U2OS or MDA-MB-231 cells (parental, MYO10 knockout or knockout but re-expressing GFP-MYO10 constructs) were first incubated in DMEM with 10% FBS medium containing 2 mM thymidine for 16 h, removed thymidine by washing cells with phosphate buffered saline (PBS) three times, incubated in fresh DMEM with 10% FBS culture media for 9 h, and a second round of thymidine was added and incubated for 16 h. The media was again removed, and the cells were washed with PBS three times, and incubated in normal growth medium for different time points for sample collection. A549 cells were similarly synchronized except at 2.5 mM thymidine.

Most experiments were analyzed between 8 and 13 h post release unless specified; however, to analyze cytokinesis, specifically the presence of intercellular bridge, cells were evaluated between 14 and 16 h post release.

**Clonogenic survival assay—**Cell survival assay was conducted as previously reported with modifications.[69,70] To determine the sensitivity of cells to taxol, 40,000 cells were plated in 2 mL medium in a 6-well plate overnight and added different concentrations of taxol dissolved in DMSO. After 12 h of treatment, cells were harvested using trypsin and washed three times with PBS. About 2000 cells were re-plated into 12-well plates in triplicate, and the cells were allowed to grow for ~12 days in drug-free media at 37°C. Colony staining was performed with 1 mL of crystal violet solution (0.5% w/v crystal violet, in methanol) at room temperature for 30 min, washed under tap water, placed upside down for air drying. After scanning, the colonies were dissolved using 1% SDS, and the absorbance at 570 nm was measured.

**cGAMP measurement by enzyme-linked immunosorbent assay (ELISA)—**The content of cGAMP in cells was measured by the cGAMP ELISA kit (#501700) purchased from Cayman Chemical (Ann Arbor, MI, USA) according to the manufacturer's protocol. In brief, MDA-MB-231 parental, MYO10$^{+/-}$, MYO10$^{+/-}$ cells re-expressing GFP-MYO10 (WT, S1062R, L1063P, or S1066A) were seeding in 60 mm culture dishes. The next day, cells were harvested using cell scraper and lysed in 0.2% PBS on ice. After centrifuging at 10,000 g for 10 min at 4°C, the supernatants were collected for ELISA analysis.

**Mass spectrometry identification of MYO10 phosphorylation sites—**To determine phosphorylation sites for MYO10, A549 cells were plated in three 10 cm dishes and cultured at 37°C for 36 h to reach about 90% confluency. The cells were washed twice with PBS and collected using a cell scraper. After centrifugation at 800 g for 5 min at 4°C, the pellet was suspended in Nonidet P-40 (NP40) lysis buffer containing 50 mM Tris-HCl pH 7.6, 150 mM NaCl, 10 mM NaF and 0.5% NP40, supplemented with 1 mM PMSF, 1 mM DTT, 10 μg/mL aprotinin, and 1 μg/mL leupeptin. Samples were incubated for 30 min on ice, sonicated using three rounds of 15/10 on/off cycles, centrifuged at 10,000 g at 4°C for 10 min. The concentration of proteins in the supernatant was measured and 4 μg of lysates were incubated with 4 μg monoclonal MYO10 antibody overnight. Next day, 50 μL Protein A/G agarose beads were added to the supernatant and incubated for another 2 h at 4°C. Beads were washed three times with lysis buffer, bound MYO10 was eluted with SDS sample buffer, and the elute was run on 6% SDS-polyacrylamide gel electrophoresis (PAGE) for 10 min. The gel bands were excised and subjected to in-gel digestion by chymotrypsin.

The digest was analyzed by LC-MS/MS using a Thermo Scientific Fusion Lumos mass spectrometer system. Liquid chromatography was carried out using an Acclaim Pepmap C18 column (75 μm × 25 cm, C18, 2μm, 100 Å, Thermo Fisher Scientific). Peptides were chromatographed with a linear acetonitrile gradient from 2% to 35% in aqueous 0.1% formic acid over 110 min at 300 nL/min. The effluent was introduced into the micro electrospray ion source of the mass spectrometer. Samples were analyzed by data-dependent MS/MS with CID fragmentation. Full MS scanning was performed at 120,000 resolution between m/z 350 and 1500, and MS/MS spectra were collected in the ion trap.

Phosphorylated peptides were identified by comparing all the experimental peptide MS/MS spectra against the amino acid sequence of MYO10 using Mascot database search software (version 2.4, Matrix Science, London, UK). Carbamidomethylation of cysteine was set as

a fixed modification, whereas variable modifications included phosphorylation of Ser, Thr, and Tyr and oxidation of methionine-to-methionine sulfoxide. The mass tolerance was set at 10 ppm for precursor ions and 0.5 Da for product ions.

**Monoclonal anti-pMYO10 antibody production—**To produce antibodies recognizing S1060/S1062/S1066 phosphorylated human MYO10, a phospho-peptide CQDpSGpSLHNpSSSGE and a control non-phosphorylated peptide CQDSGSLHNSSSGE were synthesized by Thermo Fisher/Life Technologies Corp (Carlsbad, CA, USA), in which a cysteine residue was added to the N-terminus for subsequent Keyhole limpet haemocyanin (KLH) conjugation and immunogenicity in mice. The purify of synthesized peptide was confirmed to be >95% by HPLC.

For antibody generation, eight 4–6 week-old Balb/c female mice were injected intra-peritoneally with an emulsion containing the target phosphor-peptide four times with 2–3 weeks apart. A fifth final boost was done 4 weeks after the fourth injection. Serum titers were measured by ELISA after the third and fourth injections. The spleens from the two highest tier mice were isolated, pooled, and spleen cells were isolated to fuse with an SP2/0 myeloma cell line obtained from ATCC using a standard polyethylene glycol (PEG) protocol. Fused cells were selected using hypoxanthine aminopterin thymidine (HAT) media. Twelve days later, supernatants were removed and assayed in a separate ELISA for the phosphor-peptide and the control non-phospho-peptide. The highest hits that were specific to the phosphor-peptide, but not the non-phospho-peptide, were expanded and re-assayed by Western blotting to recognize MYO10. Cells from positive wells were expanded for cloning using a limited dilution method.

The clone 2C10–6 was chosen for large scale antibody (IgG1 type) production as it generated the strongest and clear signal for the phosphor-peptide, but not the non-phosphor peptide, in the ELISA screening, which was validated by Western blot. Briefly, the hybridoma was moved to one well of a 24-well plate in DMEM with 5% FBS. In a 2-week interval, serum concentration was reduced to zero and the DMEM was changed to serum-free CD media (Tissue Culture Core lab, Lerner Research, Cleveland Clinic). Once in serum-free media, the cells were expanded to three T162 $cm^2$ flasks (Costar). Cells from these flasks were used to seed a Celline 1000 Integra Flask (Wheaton) to collect the antibodies. The ascites was filtered through a 0.22 μm filter and used for immune detection.

**Western blot analysis—**Western blot analyses were performed as previously reported with modifications.[71–73] Briefly, whole cell lysates were prepared by incubating cells in NP40 buffer (50 mM Tris-HCl pH 7.6, 200 mM NaCl, 10 mM NaF, and 1% Nonidet P-40) supplemented with 1 mM PMSF, 1 mM DTT, 10 μg/mL aprotinin, and 1 μg/mL leupeptin. After lysis on ice for 30 min, samples were sonicated for two cycles of a 10-s on/off cycle using a QSONICA Sonicator, and centrifuged at 10,000 g for 10 min at 4°C. The supernatant was collected, and protein concentration was measured using the BCA protein assay kit (#23225) from Pierce/Thermo Scientific. Lysates were boiled at 95°C for 5 min and equal amount of proteins were separated using 6%, 10% and 15% gradient SDS-PAGE, transferred to methanol-activated polyvinylidene difluoride (PVDF) membrane (Immobilon, Millipore, Bedford, MA). The membranes were blocked with 2% dry milk at

room temperature for 30 min, and incubated with primary antibodies (1:1000 dilution in TBS Tween buffer for all purified antibodies; 1:50 for pMYO10 ascites and 1:500 for anti-Ub) overnight at 4°C and subsequently incubated with HRP-labeled secondary antibodies (1:5000–1:100000) at room temperature for 1 h, washed and reacted with ECL solution, and images were taken under the Tanon 5200 Imager system (Tanon Inc, Shanghai, China).

**Immunoprecipitation—**GFP-MYO10 WT or mutants and Flag-β-TrCP1 constructs were transfected to HEK293T cells for 48 h. Cell lysates were obtained as described above, incubated three mg of proteins with the anti-GFP antibody overnight at 4°C. The next day, Protein A/G Sepharose beads (40 μL) was added to the samples and incubated for 3 h at 4°C with gentle rotation. Immunoprecipitated proteins were collected by centrifugation, washed five times using the same lysis buffer, boiled in 40 μL 2X SDS sample loading buffer, and subjected to SDS-PAGE. For endogenous protein immunoprecipitation, at least $2\times10^6$ cells were lysed in 1 mL of NP40 lysis buffer on ice for 30 min, and briefly sonicated (2% power output, 5 s per cycle for 2 cycles). After cell lysates were centrifuged at 10,000 g for 10 min at 4°C, supernatants were incubated with primary antibodies (1 μg/1 mg lysates) overnight at 4°C, which then were processed similarly.

**Immunofluorescence—**Immunofluorescence was conducted as previously reported.[35,74] U2OS or MDA-MB-231 parental, $MYO10^{+/-}$, and $MYO10^{+/-}$ cells expressing GFP-MYO10 WT or mutants were cultured in 6-well plates with #1.0 glass coverslips (#1254580, Thermo Fisher). To analyze cells in mitosis, we used two immunofluorescence protocols. In most experiments, cells were fixed with 4% paraformaldehyde for 15 min at room temperature and washed with PBS for 5 min three times. Cells were then permeabilized with 0.5% (vol/vol) Triton X-100/PBS for 30 min. After washed for 10 min three times, coverslips were incubated in blocking buffer (10% FBS, 0.2% bovine serum albumin in 0.1% Triton X-100/PBS) for 30 min to prevent non-specific antibody binding. After blocking and washing, coverslips were incubated overnight at 4°C with primary antibodies (pMYO10, 1:30 dilution; MYO10,1:50 dilution; Pericentrin, 1:2000 dilution; α-Tubulin, 1:50; γ-Tubulin, 1:250 dilution) in 0.1% Triton X-100/PBS. The coverslips were washed for 10 min in 0.1% Triton X-100/PBS three times, and incubated with secondary antibody (anti-rabbit or anti-mouse Alexa Fluor 488 or Alexa Fluor 594, 1:1000 dilution) at room temperature for 1.5 h. After washing for 10 min in 0.1% Triton X-100/PBS three times, coverslips were mounted onto glass slides with ProLong Antifade mounting solution containing 4′,6-diamidino-2-phenylindole (DAPI) (#P36931, from Life Technologies/Thermo Fisher, Carlsbad, CA, USA), and visualized under fluorescence microscope.

In the second approach to analyze endogenous MYO10 and pMYO10 localization through mitosis, cells grown on glass coverslips were first treated with a mild buffer (10 mM HEPES pH 7.9, 10 mM KCl, 1.5 mM MgCl2, 0.34 M sucrose, 10% glycerol and protease inhibitors) to remove the cytosolic components for 5 min at 4°C. Cells were then washed with 0.1% Tween in PBS for 2 min three times, fixed with 4% paraformaldehyde for 15 min, washed with PBS and the samples were processed as stated in the Methods.

**Centrosome size analysis—**Cells labeled with pMYO10 or Pericentrin in immunofluorescence images were observed with a DM6000B Leica fluorescence

microscope (Nuhsbaum Inc) that has integrated a QImaging Retiga EXi CCD digital camera (Fast 1394). The data obtained were acquired with a 100x objective oil lens, using the same exposure time for each captured image. For the analysis of the intensity of pMYO10 or Pericentrin signal in centrosome, cells were first selected and grouped according to the stage of mitosis in which cells were found. For two-dimensional area acquisition, a boundary around the centrosomes of metaphase cells was drawn in ImageJ/FIJI. Next, the total intensity was calculated by multiplying the obtained area and intensity, which was then normalized to that in prophase stage.

**Tumor mouse xenografts—**Xonograft mouse tumor studies were conducted as previously reported with modifications.[75] To establish tumor xenografts, $5\times10^6$ MDA-MB-231 parental, $MYO10^{+/-}$, $MYO10^{+/-}$ cells stably expressing GFP-MYO10 (WT, S1060A, S1062R, L1063P, and S1066A) were suspended in Matrigel: serum free DMEM medium (1:1 ratio) and implanted into the mammary fat pad of 8-week-old female nude mice (#002019) purchased from the Jackson Laboratory (Bar Harbor, ME, USA). Each group contained five mice. Tumors were monitored one week after implantation, and measured twice a week to obtain the tumor length (L) and width (W). To determined Tumor volume, a formula [$(L \times W2)/2$ $mm^3$] was used.

Mouse studies were approved by the Institutional Animal Care and Use Committee (IACUC) at Case Western Reserve University and are consistent with the recommendations of the American Veterinary Medical Association (AVMA) Guidelines on Euthanasia before the initiation of experiments. Mice were housed in group (four per cage) with bedding, controlled temperature (23 ± 2°C), humidity (50 ± 5%) and illumination (12 h light/dark cycle). Mice were maintained for one week to adapt to the facility before experiments.

**RNA extraction and qPCR from mouse tumor tissues—**qPCR was performed as previously described[69,76] and followed the minimum information for publication of quantitative real-time PCR (MIQE) guidelines. Total RNA was isolated using Trizol and chloroform extraction. The supernatant obtained after centrifugation was combined with 100% ethanol and then transferred to columns of RNeasy Mini Kit (Qiagen, Crawley, UK). Samples were treated with DNase (Qiagen) before reverse transcription, which was performed with 0.5 μg of total RNA in a 20 μL reaction containing regents from the Revert Aid first-strand cDNA synthesis kit (#K1622, Thermo Fisher Scientific). qPCR amplification was performed in triplicate using the SYBR Green Master Mix (#208054) from Invitrogen/Thermo Fisher Scientific (Franklin, MA, USA) on the Bio-Rad CFX96 Real-Time System (Bio-Rad Laboratories). qPCR quantitation was normalized to the level of endogenous control β-Actin. The specific primers used are reported in Table S1.

## QUANTIFICATION AND STATISTICAL ANALYSIS

Data are presented as median and standard deviation or unless indicated from at least three independent values. Randomization does not apply to our analyses, because cell lines and/or treatment conditions were per-determined. Specifically, each cell line or treatment is specifically defined (overexpressing a particular protein or with a specific manipulation like gene depletion or agent treatment). Blinding was not used in our analyses, because the

groups of each experiment were pre-determined and collected into distinct settings. Hence, we analyzed all collected samples based on their per-determined groups and each group has been clearly defined. No statistical methods or criteria were used to estimate sample size or to include or exclude samples.

All statistical analyses were performed by the GraphPad Prism software version 9.0 (GraphPad Software, CA, USA). When normalized control group was included to perform statistical analysis, non-parametric Mann–Whitney *U* test analysis was used. For non-normalized values, unpaired two-tailed t test was conducted to determine the difference between the control group and the treatment group at the same experimental setting. One-way ANOVA test was applied to compare two or multiple groups comparison. All quantitation methods are described in the Methods section or in the figure legends. p-values of less than at least 0.05 were considered statistically significant.

## Supplementary Material

Refer to Web version on PubMed Central for supplementary material.

## ACKNOWLEDGMENTS

We thank Melanie Hoffner and Earl Poptic at the Hybridoma Core at the Lerner Research Institute for generating the mouse monoclonal antibody recognizing phosphorylated MYO10. We thank Belinda Willard and Ling Li at the Lerner Research Institute for the acquisition of mass spectrometry data. The mass spectrometer used in the study was purchased with an NIH Shared Instrument Grant (S10 RR031537). Y.Z. was supported by NCI/NIH (CA230453), the Clinical and Translational Science Collaborative (CTSC) of Cleveland UL1TR000439 from the NCATS NIH, an institutional VeloSano Bike to Cure Pilot grant, and a Case Comprehensive Cancer Center Pilot grant (P30CA043703).

## INCLUSION AND DIVERSITY

We worked to ensure diversity in experimental samples through the selection of the cell lines.

## REFERENCES

1. Kops Geert JPL, Weaver BAA, and Cleveland DW (2005). On the road to cancer: aneuploidy and the mitotic checkpoint. Nat. Rev. Cancer 5, 773–785. 10.1038/nrc1714. [PubMed: 16195750]
2. Holland AJ, and Cleveland DW (2009). Boveri revisited: chromosomal instability, aneuploidy and tumorigenesis. Nat. Rev. Mol. Cell Biol. 10, 478–487. 10.1038/nrm2718. [PubMed: 19546858]
3. Debec A, Sullivan W, and Bettencourt-Dias M (2010). Centrioles: active players or passengers during mitosis? Cell. Mol. Life Sci. 67, 2173–2194. 10.1007/s00018-010-0323-9. [PubMed: 20300952]
4. Pihan GA (2013). Centrosome dysfunction contributes to chromosome instability, chromoanagenesis, and genome reprograming in cancer. Front. Oncol. 3, 277. 10.3389/fonc.2013.00277. [PubMed: 24282781]
5. Pihan GA, Wallace J, Zhou Y, and Doxsey SJ (2003). Centrosome abnormalities and chromosome instability occur together in pre-invasive carcinomas. Cancer Res. 63, 1398–1404. [PubMed: 12649205]
6. Gavet O, and Pines J (2010). Activation of cyclin B1-Cdk1 synchronizes events in the nucleus and the cytoplasm at mitosis. J. Cell Biol. 189, 247–259. 10.1083/jcb.200909144. [PubMed: 20404109]
7. Jackman M, Lindon C, Nigg EA, and Pines J (2003). Active cyclin B1-Cdk1 first appears on centrosomes in prophase. Nat. Cell Biol. 5, 143–148. 10.1038/ncb918. [PubMed: 12524548]

8. Portier N, Audhya A, Maddox PS, Green RA, Dammermann A, Desai A, and Oegema K (2007). A microtubule-independent role for centrosomes and aurora a in nuclear envelope breakdown. Dev. Cell 12, 515–529. 10.1016/j.devcel.2007.01.019. [PubMed: 17419991]
9. Green RA, Paluch E, and Oegema K (2012). Cytokinesis in animal cells. Annu. Rev. Cell Dev. Biol. 28, 29–58. 10.1146/annurev-cellbio-101011-155718. [PubMed: 22804577]
10. Kollmar M, and Mühlhausen S (2017). Myosin repertoire expansion coincides with eukaryotic diversification in the Mesoproterozoic era. BMC Evol. Biol. 17, 211. 10.1186/s12862-017-1056-2. [PubMed: 28870165]
11. Tokuo H (2020). Myosin X. Adv. Exp. Med. Biol. 1239, 391–403. 10.1007/978-3-030-38062-5_17. [PubMed: 32451868]
12. Matsumura F, Yamakita Y, and Yamashiro S (2011). Myosin light chain kinases and phosphatase in mitosis and cytokinesis. Arch. Biochem. Biophys. 510, 76–82. 10.1016/j.abb.2011.03.002. [PubMed: 21396909]
13. Kerber ML, and Cheney RE (2011). Myosin-X: a MyTH-FERM myosin at the tips of filopodia. J. Cell Sci. 124, 3733–3741. 10.1242/jcs.023549. [PubMed: 22124140]
14. Nagy S, Ricca BL, Norstrom MF, Courson DS, Brawley CM, Smithback PA, and Rock RS (2008). A myosin motor that selects bundled actin for motility. Proc. Natl. Acad. Sci. USA 105, 9616–9620. 10.1073/pnas.0802592105. [PubMed: 18599451]
15. Ricca BL, and Rock RS (2010). The stepping pattern of myosin X is adapted for processive motility on bundled actin. Biophys. J. 99, 1818–1826. 10.1016/j.bpj.2010.06.066. [PubMed: 20858426]
16. Sun Y, Sato O, Ruhnow F, Arsenault ME, Ikebe M, and Goldman YE (2010). Single-molecule stepping and structural dynamics of myosin X. Nat. Struct. Mol. Biol. 17, 485–491. 10.1038/nsmb.1785. [PubMed: 20364131]
17. Weber KL, Sokac AM, Berg JS, Cheney RE, and Bement WM (2004). A microtubule-binding myosin required for nuclear anchoring and spindle assembly. Nature 431, 325–329. 10.1038/nature02834. [PubMed: 15372037]
18. Woolner S, O'Brien LL, Wiese C, and Bement WM (2008). Myosin-10 and actin filaments are essential for mitotic spindle function. J. Cell Biol. 182, 77–88. 10.1083/jcb.200804062. [PubMed: 18606852]
19. Hirano Y, Hatano T, Takahashi A, Toriyama M, Inagaki N, and Hakoshima T (2011). Structural basis of cargo recognition by the myosin-X MyTH4-FERM domain. EMBO J. 30, 2734–2747. 10.1038/emboj.2011.177. [PubMed: 21642953]
20. Iwano S, Satou A, Matsumura S, Sugiyama N, Ishihama Y, and Toyoshima F (2015). PCTK1 regulates integrin-dependent spindle orientation via protein kinase A regulatory subunit KAP0 and myosin X. Mol. Cell Biol. 35, 1197–1208. 10.1128/MCB.01017-14. [PubMed: 25605337]
21. Toyoshima F, and Nishida E (2007). Integrin-mediated adhesion orients the spindle parallel to the substratum in an EB1- and myosin X-dependent manner. EMBO J. 26, 1487–1498. 10.1038/sj.emboj.7601599. [PubMed: 17318179]
22. Zhang H, Berg JS, Li Z, Wang Y, Lång P, Sousa AD, Bhaskar A, Cheney RE, and Strömblad S (2004). Myosin-X provides a motor-based link between integrins and the cytoskeleton. Nat. Cell Biol. 6, 523–531. 10.1038/ncb1136. [PubMed: 15156152]
23. Kwon M, Bagonis M, Danuser G, and Pellman D (2015). Direct microtubule-binding by myosin-10 orients centrosomes toward retraction fibers and subcortical actin clouds. Dev. Cell 34, 323–337. 10.1016/j.devcel.2015.06.013. [PubMed: 26235048]
24. Sandquist JC, Larson ME, Woolner S, Ding Z, and Bement WM (2018). An interaction between myosin-10 and the cell cycle regulator Wee1 links spindle dynamics to mitotic progression in epithelia. J. Cell Biol. 217, 849–859. 10.1083/jcb.201708072. [PubMed: 29321170]
25. Kenchappa RS, Mistriotis P, Wisniewski E, Bhattacharya S, Kulkarni T, West R, Luu A, Conlon M, Heimsath E, Crish JF, et al. (2020). Myosin 10 regulates invasion, mitosis, and metabolic signaling in glioblastoma. iScience 23, 101802. 10.1016/j.isci.2020.101802. [PubMed: 33299973]
26. Yim YIP, Pedrosa A, Xu X, Cheney RE, and Hammer JA (2022). Myosin 10 supports mitotic spindle bipolarity by promoting PCM integrity and supernumerary centrosome clustering. Preprint at bioRxiv. 10.1101/2022.02.08.479580.

27. Mayca Pozo F, Geng X, Tamagno I, Jackson MW, Heimsath EG, Hammer JA, Cheney RE, and Zhang Y (2021). MYO10 drives genomic instability and inflammation in cancer. Sci. Adv. 7, eabg6908. 10.1126/sciadv.abg6908. [PubMed: 34524844]

28. Courson DS, and Cheney RE (2015). Myosin-X and disease. Exp. Cell Res. 334, 10–15. 10.1016/j.yexcr.2015.03.014. [PubMed: 25819274]

29. Zhang YW, Brognard J, Coughlin C, You Z, Dolled-Filhart M, Aslanian A, Manning G, Abraham RT, and Hunter T (2009). The F box protein Fbx6 regulates Chk1 stability and cellular sensitivity to replication stress. Mol. Cell 35, 442–453. [PubMed: 19716789]

30. Zhang YW, Otterness DM, Chiang GG, Xie W, Liu YC, Mercurio F, and Abraham RT (2005). Genotoxic stress targets human Chk1 for degradation by the ubiquitin-proteasome pathway. Mol. Cell 19, 607–618. 10.1016/j.molcel.2005.07.019. [PubMed: 16137618]

31. Rechsteiner M, and Rogers SW (1996). PEST sequences and regulation by proteolysis. Trends Biochem. Sci. 21, 267–271. [PubMed: 8755249]

32. Skaar JR, Pagan JK, and Pagano M (2013). Mechanisms and function of substrate recruitment by F-box proteins. Nat. Rev. Mol. Cell Biol. 14, 369–381. 10.1038/nrm3582. [PubMed: 23657496]

33. Wang Z, Liu P, Inuzuka H, and Wei W (2014). Roles of F-box proteins in cancer. Nat. Rev. Cancer 14, 233–247. 10.1038/nrc3700. [PubMed: 24658274]

34. Han X, Zhang L, Chung J, Mayca Pozo F, Tran A, Seachrist DD, Jacobberger JW, Keri RA, Gilmore H, and Zhang Y (2014). UbcH7 regulates 53BP1 stability and DSB repair. Proc. Natl. Acad. Sci. USA 111, 17456–17461. 10.1073/pnas.1408538111. [PubMed: 25422456]

35. Mayca Pozo F, Tang J, Bonk KW, Keri RA, Yao X, and Zhang Y (2017). Regulatory cross-talk determines the cellular levels of 53BP1 protein, a critical factor in DNA repair. J. Biol. Chem. 292, 5992–6003. 10.1074/jbc.M116.760645. [PubMed: 28255090]

36. Frescas D, and Pagano M (2008). Deregulated proteolysis by the F-box proteins SKP2 and beta-TrCP: tipping the scales of cancer. Nat. Rev. Cancer 8, 438–449. 10.1038/nrc2396. [PubMed: 18500245]

37. Winston JT, Koepp DM, Zhu C, Elledge SJ, and Harper JW (1999). A family of mammalian F-box proteins. Curr. Biol. 9, 1180–1182. 10.1016/S0960-9822(00)80021-4. [PubMed: 10531037]

38. Tokuo H, Bhawan J, and Coluccio LM (2018). Myosin X is required for efficient melanoblast migration and melanoma initiation and metastasis. Sci. Rep. 8, 10449. 10.1038/s41598-018-28717-y. [PubMed: 29993000]

39. Motwani M, Pesiridis S, and Fitzgerald KA (2019). DNA sensing by the cGAS-STING pathway in health and disease. Nat. Rev. Genet. 20, 657–674. 10.1038/s41576-019-0151-1. [PubMed: 31358977]

40. Nakayama K, Hatakeyama S, Maruyama S.i., Kikuchi A, Onoé K, Good RA, and Nakayama KI (2003). Impaired degradation of inhibitory subunit of NF-kappa B (I kappa B) and beta-catenin as a result of targeted disruption of the beta-TrCP1 gene. Proc. Natl. Acad. Sci. USA 100, 8752–8757. 10.1073/pnas.1133216100. [PubMed: 12843402]

41. Kudo Y, Guardavaccaro D, Santamaria PG, Koyama-Nasu R, Latres E, Bronson R, Yamasaki L, and Pagano M (2004). Role of F-box protein betaTrcp1 in mammary gland development and tumorigenesis. Mol. Cell Biol. 24, 8184–8194. 10.1128/MCB.24.18.8184-8194.2004. [PubMed: 15340078]

42. Ougolkov A, Zhang B, Yamashita K, Bilim V, Mai M, Fuchs SY, and Minamoto T (2004). Associations among beta-TrCP, an E3 ubiquitin ligase receptor, beta-catenin, and NF-kappaB in colorectal cancer. J. Natl. Cancer Inst. 96, 1161–1170. 10.1093/jnci/djh219. [PubMed: 15292388]

43. Xu J, Zhou W, Yang F, Chen G, Li H, Zhao Y, Liu P, Li H, Tan M, Xiong X, and Sun Y (2017). The beta-TrCP-FBXW2-SKP2 axis regulates lung cancer cell growth with FBXW2 acting as a tumour suppressor. Nat. Commun. 8, 14002. 10.1038/ncomms14002. [PubMed: 28090088]

44. Belaïdouni N, Peuchmaur M, Perret C, Florentin A, Benarous R, and Besnard-Guérin C (2005). Overexpression of human beta TrCP1 deleted of its F box induces tumorigenesis in transgenic mice. Oncogene 24, 2271–2276. 10.1038/sj.onc.1208418. [PubMed: 15735746]

45. Stairs DB, Nakagawa H, Klein-Szanto A, Mitchell SD, Silberg DG, Tobias JW, Lynch JP, and Rustgi AK (2008). Cdx1 and c-Myc foster the initiation of transdifferentiation of the normal

esophageal squamous epithelium toward Barrett's esophagus. PLoS One 3, e3534. 10.1371/journal.pone.0003534. [PubMed: 18953412]

46. Makowska KA, Hughes RE, White KJ, Wells CM, and Peckham M (2015). Specific myosins control actin organization, cell morphology, and migration in prostate cancer cells. Cell Rep. 13, 2118–2125. 10.1016/j.celrep.2015.11.012. [PubMed: 26670045]
47. Shi Q, and King RW (2005). Chromosome nondisjunction yields tetraploid rather than aneuploid cells in human cell lines. Nature 437, 1038–1042. 10.1038/nature03958. [PubMed: 16222248]
48. Miller DM, Thomas SD, Islam A, Muench D, and Sedoris K (2012). c-Myc and cancer metabolism. Clin. Cancer Res. 18, 5546–5553. 10.1158/1078-0432.CCR-12-0977. [PubMed: 23071356]
49. Nair UB, Joel PB, Wan Q, Lowey S, Rould MA, and Trybus KM (2008). Crystal structures of monomeric actin bound to cytochalasin D. J. Mol. Biol. 384, 848–864. 10.1016/j.jmb.2008.09.082. [PubMed: 18938176]
50. Uetake Y, and Sluder G (2004). Cell cycle progression after cleavage failure: mammalian somatic cells do not possess a "tetraploidy checkpoint. J. Cell Biol. 165, 609–615. 10.1083/jcb.200403014. [PubMed: 15184397]
51. Lens SMA, and Medema RH (2019). Cytokinesis defects and cancer. Nat. Rev. Cancer 19, 32–45. 10.1038/s41568-018-0084-6. [PubMed: 30523339]
52. Scribano CM, Wan J, Esbona K, Tucker JB, Lasek A, Zhou AS, Zasadil LM, Molini R, Fitzgerald J, Lager AM, et al. (2021). Chromosomal instability sensitizes patient breast tumors to multipolar divisions induced by paclitaxel. Sci. Transl. Med. 13, eabd4811. 10.1126/scitranslmed.abd4811. [PubMed: 34516829]
53. Duriez PJ, and Shah GM (1997). Cleavage of poly(ADP-ribose) polymerase: a sensitive parameter to study cell death. Biochem. Cell. Biol. 75, 337–349. [PubMed: 9493956]
54. Sazonova EV, Petrichuk SV, Kopeina GS, and Zhivotovsky B (2021). A link between mitotic defects and mitotic catastrophe: detection and cell fate. Biol. Direct 16, 25. 10.1186/s13062-021-00313-7. [PubMed: 34886882]
55. Anand U, Dey A, Chandel AKS, Sanyal R, Mishra A, Pandey DK, De Falco V, Upadhyay A, Kandimalla R, Chaudhary A, et al. (2022). Cancer chemotherapy and beyond: current status, drug candidates, associated risks and progress in targeted therapeutics. Genes Dis. 10.1016/j.gendis.2022.02.007.
56. Hanahan D, and Weinberg RA (2011). Hallmarks of cancer: the next generation. Cell 144, 646–674. 10.1016/j.cell.2011.02.013. [PubMed: 21376230]
57. Hanahan D (2022). Hallmarks of cancer: new dimensions. Cancer Discov. 12, 31–46. 10.1158/2159-8290.CD-21-1059. [PubMed: 35022204]
58. Willems E, Dedobbeleer M, Digregorio M, Lombard A, Lumapat PN, and Rogister B (2018). The functional diversity of Aurora kinases: a comprehensive review. Cell Div. 13, 7. 10.1186/s13008-018-0040-6. [PubMed: 30250494]
59. Sandquist JC, Larson ME, and Hine KJ (2016). Myosin-10 independently influences mitotic spindle structure and mitotic progression. Cytoskeleton (Hoboken) 73, 351–364. 10.1002/cm.21311. [PubMed: 27220038]
60. Zasadil LM, Britigan EMC, and Weaver BA (2013). 2n or not 2n: aneuploidy, polyploidy and chromosomal instability in primary and tumor cells. Semin. Cell Dev. Biol. 24, 370–379. 10.1016/j.semcdb.2013.02.001. [PubMed: 23416057]
61. Silk AD, Zasadil LM, Holland AJ, Vitre B, Cleveland DW, and Weaver BA (2013). Chromosome missegregation rate predicts whether aneuploidy will promote or suppress tumors. Proc. Natl. Acad. Sci. USA 110, E4134–E4141. 10.1073/pnas.1317042110. [PubMed: 24133140]
62. Zasadil LM, Britigan EMC, Ryan SD, Kaur C, Guckenberger DJ, Beebe DJ, Moser AR, and Weaver BA (2016). High rates of chromosome missegregation suppress tumor progression but do not inhibit tumor initiation. Mol. Biol. Cell 27, 1981–1989. 10.1091/mbc.E15-10-0747. [PubMed: 27146113]
63. Umbreit NT, Zhang CZ, Lynch LD, Blaine LJ, Cheng AM, Tourdot R, Sun L, Almubarak HF, Judge K, Mitchell TJ, et al. (2020). Mechanisms generating cancer genome complexity from a single cell division error. Science 368, eaba0712. 10.1126/science.aba0712. [PubMed: 32299917]

64. Maciejowski J, Li Y, Bosco N, Campbell PJ, and de Lange T (2015). Chromothripsis and kataegis induced by telomere crisis. Cell 163, 1641–1654. 10.1016/j.cell.2015.11.054. [PubMed: 26687355]

65. Chan PC, Hsu RYC, Liu CW, Lai CC, and Chen HC (2014). Adducin-1 is essential for mitotic spindle assembly through its interaction with myosin-X. J. Cell Biol. 204, 19–28. 10.1083/jcb.201306083. [PubMed: 24379415]

66. Peschiaroli A, Dorrello NV, Guardavaccaro D, Venere M, Halazonetis T, Sherman NE, and Pagano M (2006). SCFbetaTrCP-mediated degradation of Claspin regulates recovery from the DNA replication checkpoint response. Mol. Cell 23, 319–329. 10.1016/j.molcel.2006.06.013. [PubMed: 16885022]

67. Han X, Tang J, Wang J, Ren F, Zheng J, Gragg M, Kiser P, Park PSH, Palczewski K, Yao X, and Zhang Y (2016). Conformational change of human checkpoint kinase 1 (Chk1) induced by DNA damage. J. Biol. Chem. 291, 12951–12959. 10.1074/jbc.M115.713248. [PubMed: 27129240]

68. Zhang L, Geng X, Wang F, Tang J, Ichida Y, Sharma A, Jin S, Chen M, Tang M, Pozo FM, et al. (2022). 53BP1 regulates heterochromatin through liquid phase separation. Nat. Commun. 13, 360. 10.1038/s41467-022-28019-y. [PubMed: 35042897]

69. Wang F, Jin S, Mayca Pozo F, Tian D, Tang X, Dai Y, Yao X, Tang J, and Zhang Y (2022). Chemical screen identifies shikonin as a broad DNA damage response inhibitor that enhances chemotherapy through inhibiting ATM and ATR. Acta Pharm. Sin. B 12, 1339–1350. 10.1016/j.apsb.2021.08.025. [PubMed: 35530159]

70. Geng X, Wang F, Tian D, Huang L, Streator E, Zhu J, Kurihara H, He R, Yao X, Zhang Y, and Tang J (2020). Cardiac glycosides inhibit cancer through Na/K-ATPase-dependent cell death induction. Biochem. Pharmacol. 182, 114226. 10.1016/j.bcp.2020.114226. [PubMed: 32976831]

71. Han X, Aslanian A, Fu K, Tsuji T, and Zhang Y (2014). The interaction between checkpoint kinase 1 (Chk1) and the minichromosome maintenance (MCM) complex is required for DNA damage-induced Chk1 phosphorylation. J. Biol. Chem. 289, 24716–24723. [PubMed: 25049228]

72. Wang F, Zhang M, Yuan M, Xia Z, Yang F, Zhang S, Lin T, Luo L, Tang J, and Zhang Y (2023). A novel sorbicillinoid compound as a potent anti-inflammation agent through inducing NLRP3 protein degradation. Br. J. Pharmacol. 10.1111/bph.16058.

73. Wang J, Engle S, and Zhang Y (2011). A new in vitro system for activating the cell cycle checkpoint. Cell Cycle 10, 500–506. [PubMed: 21252628]

74. Han X, Mayca Pozo F, Wisotsky JN, Wang B, Jacobberger JW, and Zhang Y (2015). Phosphorylation of minichromosome maintenance 3 (MCM3) by checkpoint kinase 1 (Chk1) negatively regulates DNA replication and checkpoint activation. J. Biol. Chem. 290, 12370–12378. 10.1074/jbc.M114.621532. [PubMed: 25809478]

75. Tian D, Tang J, Geng X, Li Q, Wang F, Zhao H, Narla G, Yao X, and Zhang Y (2020). Targeting UHRF1-dependent DNA repair selectively sensitizes KRAS mutant lung cancer to chemotherapy. Cancer Lett. 493, 80–90. 10.1016/j.canlet.2020.08.008. [PubMed: 32814087]

76. Wang F, Mayca Pozo F, Tian D, Geng X, Yao X, Zhang Y, and Tang J (2020). Shikonin inhibits cancer through P21 upregulation and apoptosis induction. Front. Pharmacol. 11, 861. 10.3389/fphar.2020.00861. [PubMed: 32581812]

## Highlights

- MYO10 degradation depends on a degron and phosphorylation of the degron motif
- MYO10 undergoes spatiotemporal regulation during mitosis
- Degron cancer mutations abolish MYO10 phosphorylation, degradation, and mitotic regulation
- Cancers expressing high-level or stabilized MYO10 are sensitive to Taxol

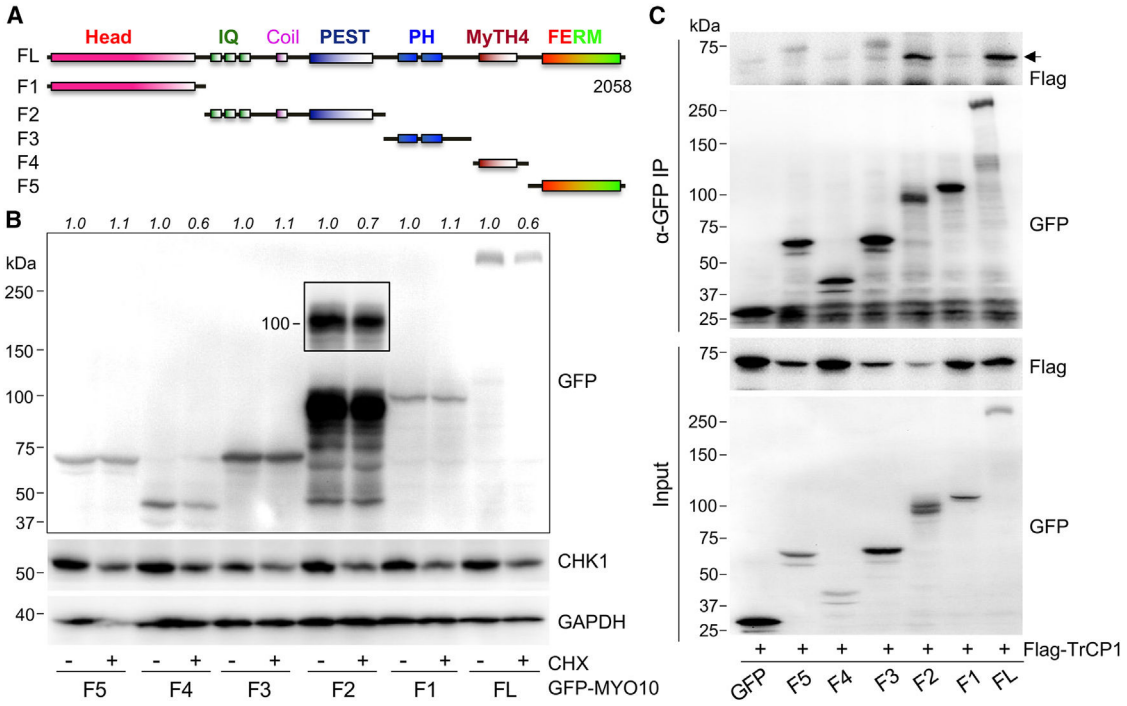


**Figure 1. Domains of MYO10 in regulating the protein stability**

(A) Schematic diagram of human MYO10 (UniProt: Q9HD67). Head: actin binding; IQs (isoleucine-glutamine): calmodulin binding; coil-coil domain: dimerization; PEST (Pro/Glu/Ser/Thr-rich): protein cleavage; PH (pleckstrin homology): PIP3 (phosphatidylinositol (3,4,5)-trisphosphate) binding; MyTH4 (myosin tail homology 4): microtubule binding; FERM (band4.1, ezrin, radixin, moesin): tubulin and β-integrin binding. The specific amino acid position of each fragment is defined by the primers described in the STAR Methods and Table S1.

(B) HEK293T cells were transfected with GFP-MYO10 FL or fragments for 48 h, treated with 320 μM CHX for 6 h, and protein levels were examined. Inset: a short exposure for F2. A representative result from more than three independent replicates is shown. Numbers represent the relative protein levels of GFP-MYO10 quantitated from the GFP blot by ImageJ.

(C) HEK293T cells were transfected with GFP-MYO10 constructs and Flag-β-TrCP1 for 48 h, subjected to coIP with anti-GFP, and blotted with indicated antibodies. The arrow indicates Flag-β-TrCP1. Protein expression in the input was also determined.

See also Figure S1.

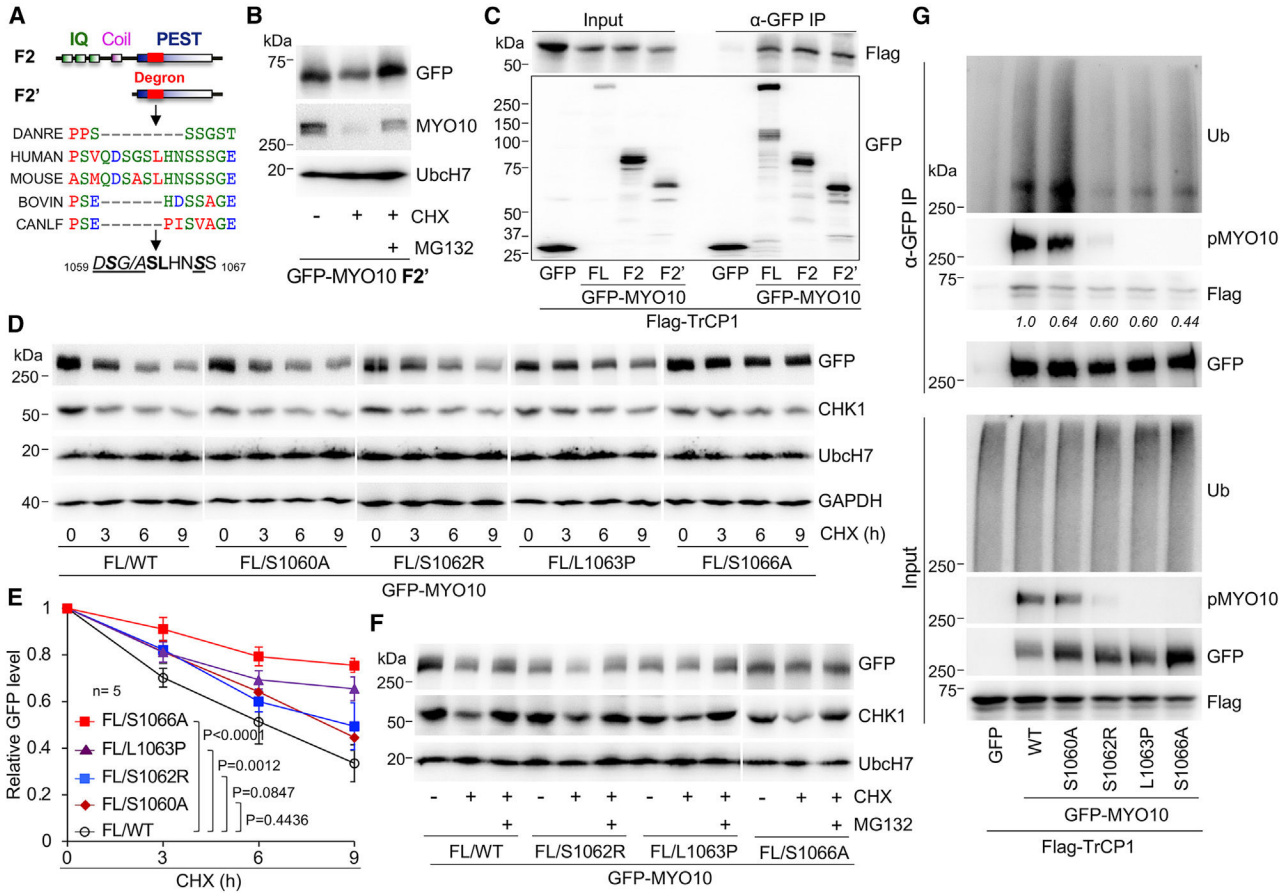


**Figure 2. Identification of phosphor-degron of MYO10**

(A) Alignment of the “degron” motif (indicated by the red rectangles) in MYO10 from different species. Numbers indicate the amino acid positions in human MYO10.

(B) HEK293T cells were transfected with GFP-MYO10-F2′ for 48 h, treated with 320 μM CHX in the presence or absence of 10 μM MG132 for 6 h, and protein expression was examined.

(C) HEK293T cells were transfected with GFP-MYO10 FL, F2 or F2′, and Flag-β-TrCP1 for 48 h and performed coIP.

(D) HEK293T cells were transfected with GFP-MYO10 FL/WT or mutants for 48 h, treated with 320 μM CHX for indicated time, and protein levels were examined. A representative result from five independent experiments is shown.

(E) The protein band intensities of the GFP blots in (D) were quantified by ImageJ and are presented as average and standard deviation after normalized to the 0-h time point, in which an equal amount of total proteins was loaded for all lanes. Statistical analysis indicates non-parametric analysis for the 9-h time point from n = 5 independent experiments.

(F) HEK293T cells were transfected with GFP-MYO10 WT or mutants for 48 h, treated with 320 μM CHX in the presence or absence of 10 μM MG132 for 6 h, and protein expression was examined.

(G) HEK293T cells were transfected with GFP-MYO10 (WT or mutants) and Flag-β-TrCP1 for 48 h, treated with 10 μM MG132 for 4 h, lysed and performed anti-GFP coIP, and blotted

with anti-pMYO10 or anti-Flag antibodies. Numbers: the band intensity of Flag-β-TrCP1 in the coIP lanes normalized to that in the corresponding input lanes and adjusted to that in the GFP-MYO10 WT group. To detect MYO10 ubiquitination, we lysed parallel samples in 1% SDS to denature protein complexes, diluted the lysates to 0.1% SDS with regular lysis buffer, carried out anti-GFP coIP, and blotted with anti-Ub antibodies. Protein expression in the input was also examined.

See also Figures S2 and S3.

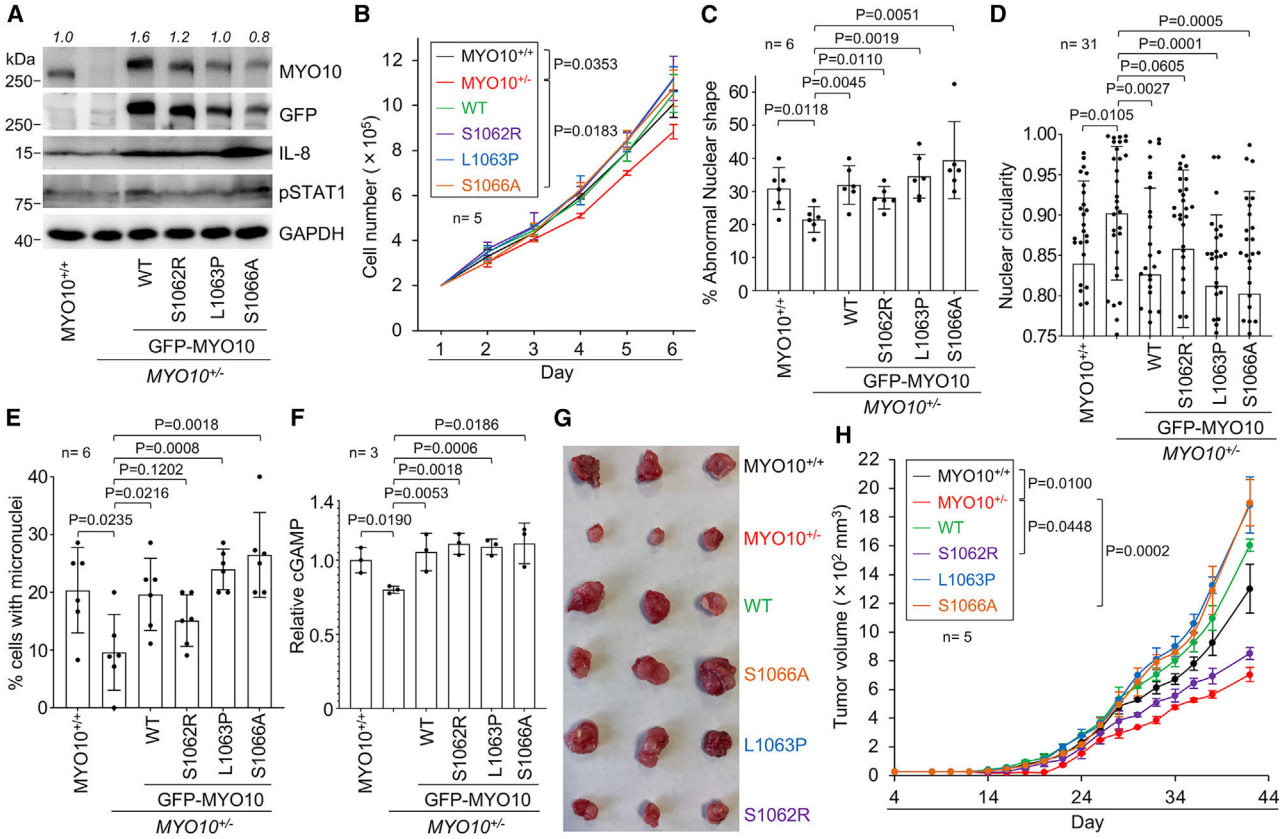


**Figure 3. Increasing or stabilizing MYO10 increases genomic instability, inflammation, and tumor growth**

(A) Protein expression in MDA-MB-231 parental, MYO10$^{+/-}$, and MYO10$^{+/-}$ cells stably expressing GFP-MYO10 WT or mutants. A representative result from two independent replicates is shown and quantitated in Figures S4A and S4B.

(B) Growth curve of cells in (A) over a period of 6 days from n = 5 replicates.

(C) Percentage of cells with abnormal nuclear shape from n = 6 images representing 62, 61, 57, 54, 56, and 55 cells for each group done in duplicate.

(D) Measurement of nuclear circularity from n = 31 cells in (A) by ImageJ.

(E) Percentage of cells with micronuclei from n = 6 images representing 43, 45, 41, 53, 55, and 30 cells for each group done in duplicate.

(F) Normalized cellular level of cGAMP from cells in (A) measured by ELISA from n = 3 replicates.

(G and H) Representative tumor images (G) and tumor growth (H) from cells in (A).

Data in (C)–(F) represent median and standard deviation, whereas data in (H) represent median and standard error of mean. Statistical analysis was conducted from indicated number (n) of cells/events/replicates by Prism 9.0, representing values from unpaired two-tailed t test in (C)–(E), non-parametric Mann-Whitney U test in (F), and one-way ANOVA test in (H). See also Figures S4 and S5.

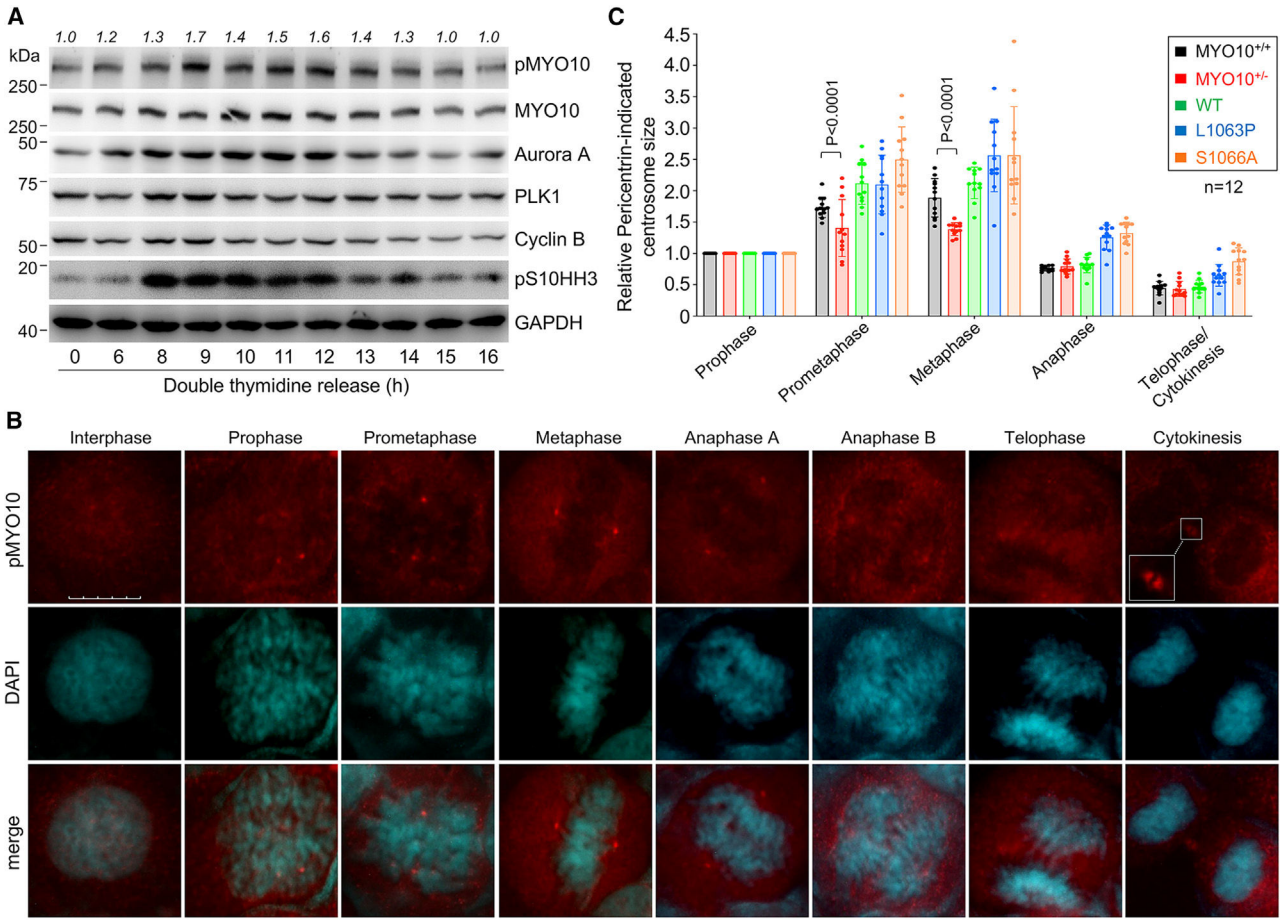


**Figure 4. Spatiotemporal regulation of pMYO10 during mitosis**

(A) A549 cells underwent a double-thymidine block and release treatment, collected at the indicated time after the second release, and protein expression was examined. The band intensity of the pMYO10 blot was quantitated by ImageJ and presented as numbers representing the relative abundance to the 0-h time point.

(B) U2OS cells were collected after 8–13 h of the second release from a double-thymidine block and release treatment, fixed, and stained with the anti-pMYO10 antibody and DAPI. Images representing different stages of mitosis were from three independent experiments. Scale bar: 10 μm. Inset: midbody.

(C) U2OS parental, MYO10$^{+/-}$, and MYO10$^{+/-}$ cells stably expressing GFP-MYO10 WT or mutants were treated the same as in (B) but stained with Pericentrin. The size of centrosomes indicated by Pericentrin was measured by ImageJ as described in the STAR Methods and Figure S7B. Data represent median and standard deviation from n = 12 cells from two independent experiments. Statistical analysis was non-parametric Mann-Whitney U test by Prism 9.0.

See also Figures S6–S10.

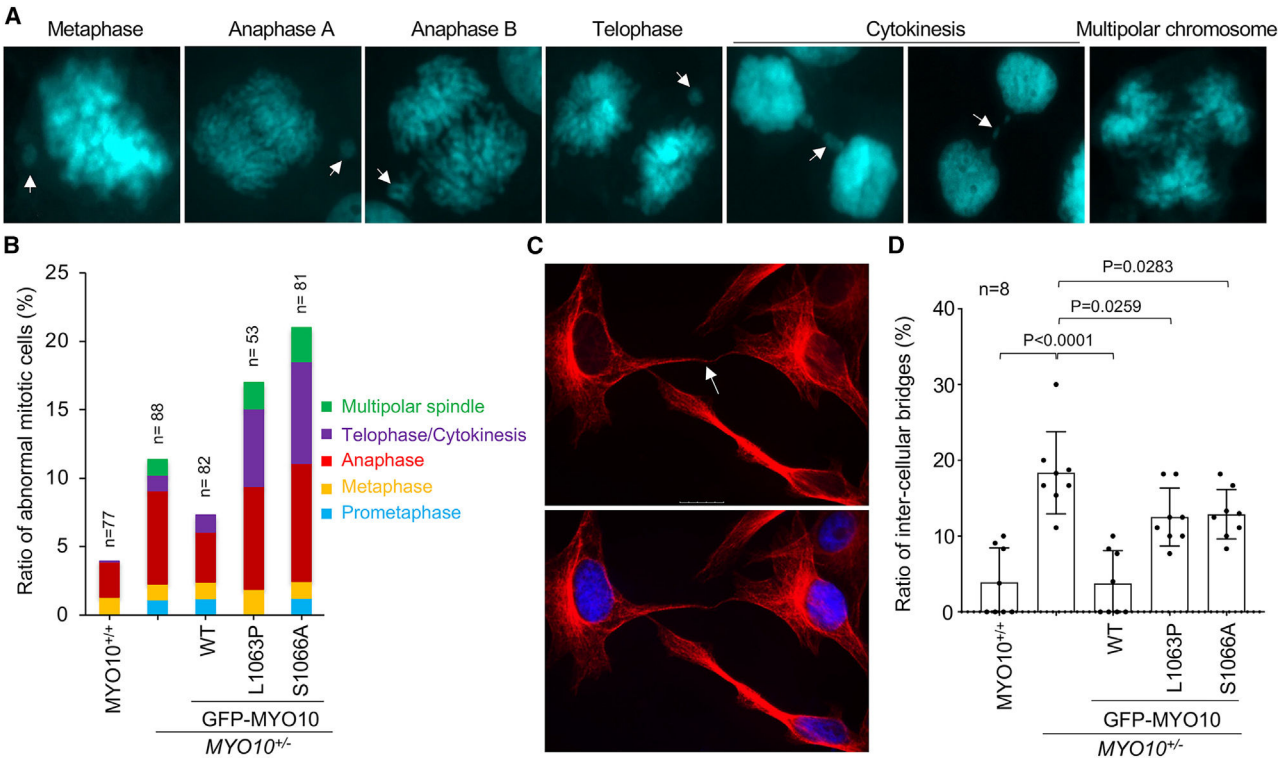


**Figure 5. MYO10 is required for maintaining genome stability through mitosis**

(A) Representative images of mitotic abnormalities in MYO10$^{+/-}$ U2OS cells from two independent experiments. Arrows indicate abnormal chromosomal DNA.

(B) U2OS parental, MYO10$^{+/-}$, and MYO10$^{+/-}$ cells stably expressing GFP-MYO10 WT or mutants were treated with a double-thymidine block and release protocol, released into drug-free media for 8–13 h, fixed, and stained with DAPI. The ratio of each type of mitotic abnormality shown in (A) was quantitated over the total number (n) of mitotic cells from two independent experiments.

(C) Parallel cell samples in (B) were fixed and stained with α-Tubulin and DAPI. A representative image of an intercellular bridge linking two MYO10$^{+/-}$ U2OS daughter cells (arrow) is shown. Scale bar: 25 μm.

(D) The ratio of cells with intercellular bridges from cells in (C). Cells that were far away (the two nuclei were ~100 μm by DAPI staining) but connected (by α-Tubulin staining) were scored. Eight images were analyzed with a total number of 158, 164, 150, 144, and 154 cells for each group from two independent experiments. Data represent median and standard deviation. Statistical analyses represent unpaired two-tailed t test.

See also Figure S11.

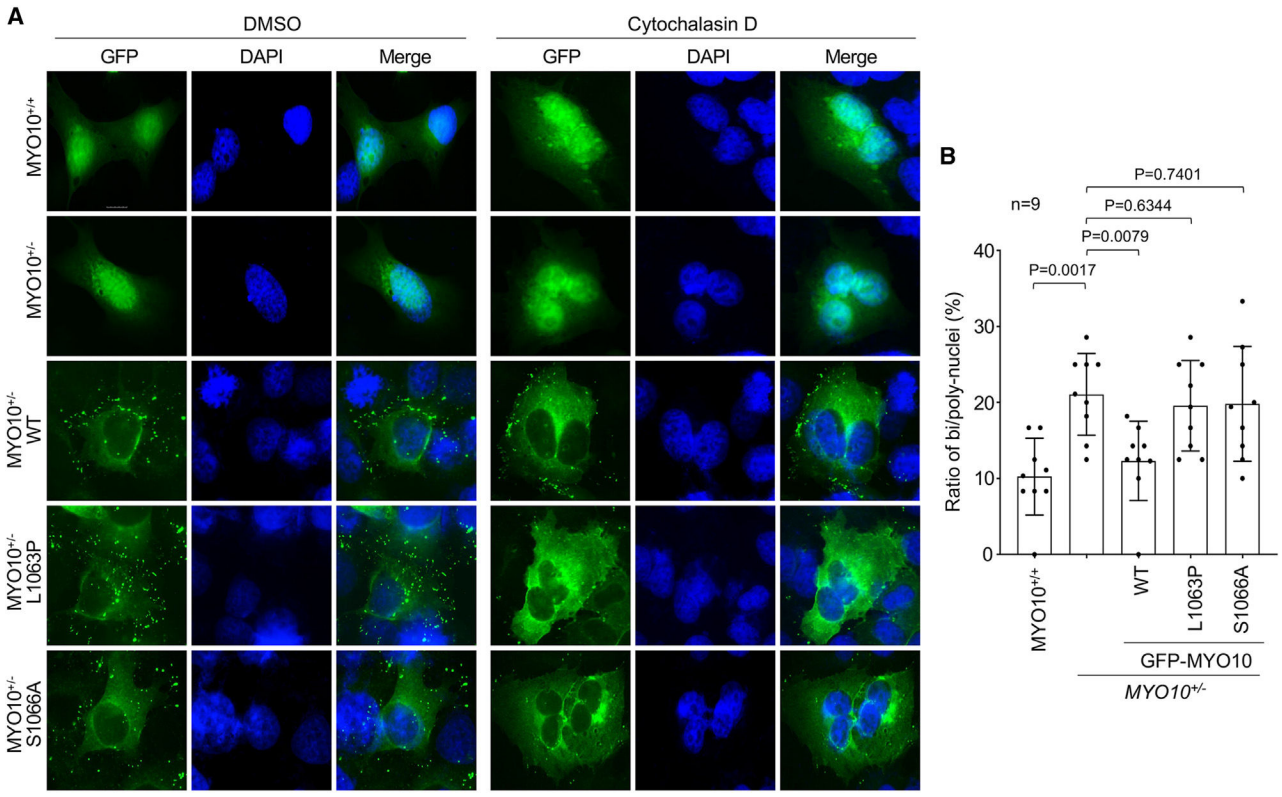


**Figure 6. MYO10 regulates cytokinesis**

(A) U2OS parental and MYO10$^{+/-}$ cells were transfected with an GFP vector for 24 h, including MYO10$^{+/-}$ cells stably expressing GFP-MYO10 WT, L1063P, or S1066A to undergo a double-thymidine block and release treatment. Right after the second release, we added 1 μM cytochalasin D for 16 h, then fixed and stained with DAPI. Representative images from two independent experiments are shown. Scale bar: 10 μm.

(B) Quantitation of the ratio of bi/poly-nuclei from cells in (A). Nine images were analyzed with total number of 87, 71, 65, 67, and 81 cells for each group. Data represent median and standard deviation. Statistical analyses represent unpaired two-tailed t test.

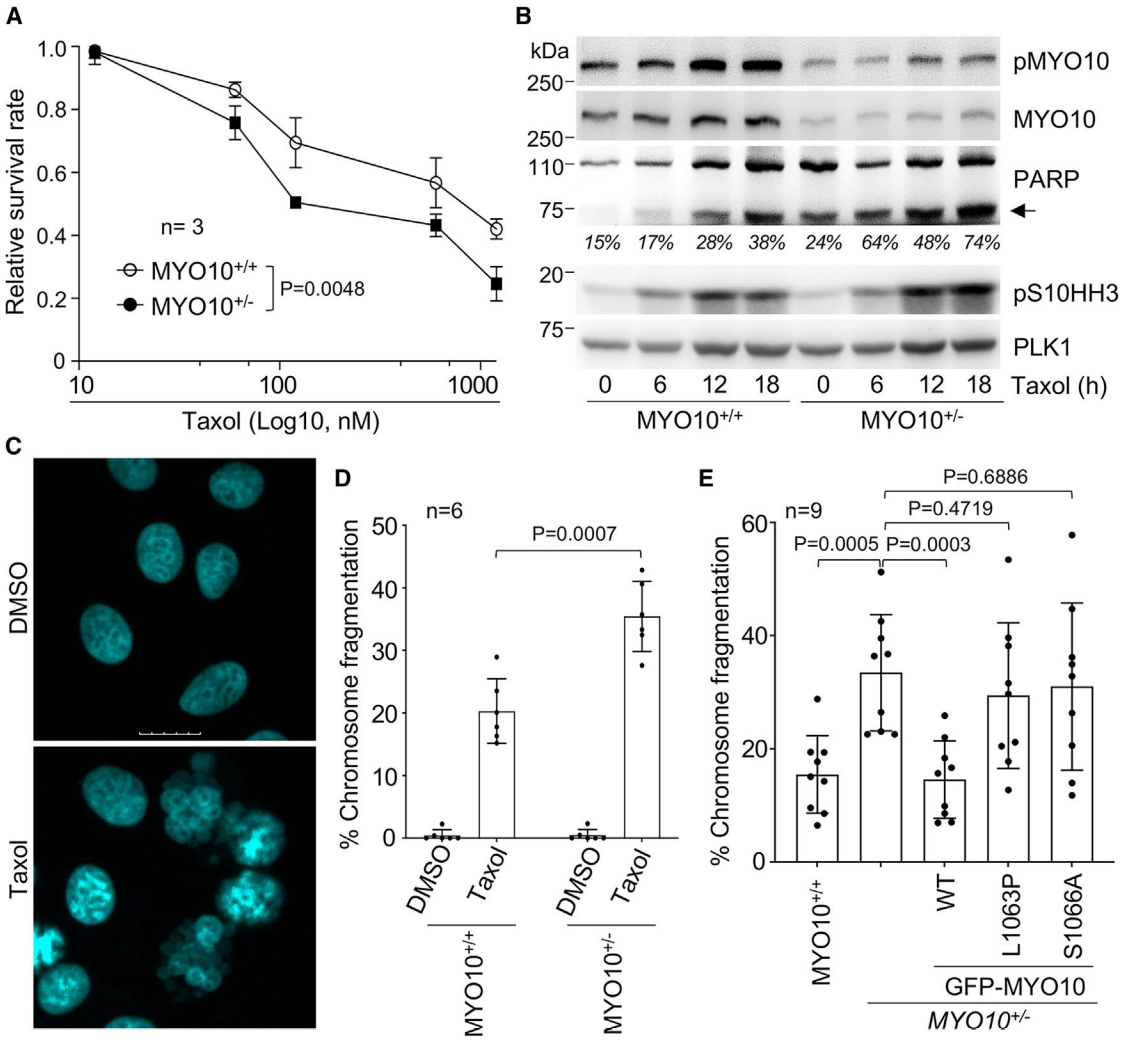


**Figure 7. MYO10 protein levels affect cellular sensitivity to Taxol**

(A) U2OS parental and MYO10$^{+/-}$ cells were treated with indicated concentrations of Taxol for 12 h, released into drug-free media and cultured for 12 days, and cell survival was assessed by quantitating the growing colonies from n = 3 replicates. One-way ANOVA was performed for statistical significance.

(B) MDA-MB-231 parental and MYO10$^{+/-}$ cells were treated with 100 nM Taxol for indicated time, and protein expression was analyzed. Arrow indicates cleaved PARP, which was quantitated by ImageJ software relative to the non-cleaved form.

(C) U2OS parental cells were treated with DMSO or 100 nM Taxol for 12 h, fixed, and stained with DAPI. Representative images are shown for fragmented chromosomes. Scale bar: 10 μm.

(D) Percentages of U2OS parental and MYO10$^{+/-}$ cells with fragmented chromosomes were counted from n = 6 samples with a total number of 262, 229, 223, and 210 cells scored for each group.

(E) U2OS parental, MYO10$^{+/-}$, and MYO10$^{+/-}$ cells stably expressing GFP-MYO10 WT or degradation-defective mutants were treated with 100 nM Taxol for 12 h, fixed, and stained

with DAPI. Percentage of cells with fragmented chromosomes was counted from n = 9 replicates with a total number of 369, 214, 349, 287, and 257 cells scored for each group. Data represent median and standard deviation for (A), (D), and (E). Statistical analyses represent unpaired two-tailed t test in (D) and (E). See also Figure S12.

## KEY RESOURCES TABLE

| REAGENT or RESOURCE | SOURCE | IDENTIFIER |
|---|---|---|
| Antibodies | | |
| Anti-MYO10 | Santa Cruz | Clone C-1, #sc-166720, mouse monoclonal, RRID: AB_2148054 |
| Anti-p-S1060/1062/1066-MYO10 | This study/Millipore/Sigma | Clone 2C10-6, #MABC1824, mouse monoclonal |
| Anti-Chk1 | Santa Cruz | Clone DCS-310, mouse monoclonal, #sc-56291, RRID: AB_1121554 |
| Anti-Lamin A/C | Santa Cruz | Clone 636, mouse monoclonal, #sc-7292, RRID: AB_627875 |
| Anti-Actin | Santa Cruz | Clone C-4, mouse monoclonal, #sc-47778, RRID: AB_626632 |
| Anti-IL-8 | Santa Cruz | Clone C-11, mouse monoclonal, #sc-376750, RRID: AB_2891256) |
| Anti-Cyclin B1 | Santa Cruz | Clone A-11, mouse monoclonal, #sc-377000, RRID: AB_2861346 |
| Anti-GFP | Bio-Techne/NOVUS Biologicals | #NB100-1770, goat polyclonal, RRID: AB_10128178 |
| Anti-UbcH7 | Bio-Techne/NOVUS Biologicals | #NB100-2265, rabbit polyclonal, RRID: AB_2304026 |
| Anti-pTBK1 | Cell Signaling Technology | Clone D52C2, Ser172, #5483S, rabbit monoclonal, RRID: AB_10693472 |
| Anti-PARP | Cell Signaling Technology | #9542S, rabbit polyclonal, RRID: AB_2160739 |
| Anti-β-TrCP1 | Cell Signaling Technology | Clone D13F10, #4394S, rabbit monoclonal, RRID: AB_10545763 |
| Anti-pSTAT1 | Cell Signaling Technology | Clone 58D6, Tyr701, #9167S, rabbit monoclonal, RRID: AB_561284 |
| Anti-Flag | Millipore/Sigma | Clone M2, #F3165, mouse monoclonal, RRID: AB_259529 |
| Anti-Ub | Millipore/Sigma | #U5379, polyclonal, RRID: AB_477667 |
| Anti-PLK1 | Millipore/Sigma | Clone 35–206, #05–844, mouse monoclonal, RRID: AB_310836 |
| Anti-phospho-Histone H3 | Millipore/Sigma | Ser10, #06–570, rabbit polyclonal, RRID: AB_310177 |
| Anti-α-Tubulin | Proteintech | #24565-1-AP for staining, rabbit polyclonal, RRID: AB_2879611 |
| Anti-GAPDH | Proteintech | Clone 1E6D9, #60004-1-Ig, mouse monoclonal, RRID: AB_2107436 |
| Anti-GFP | Proteintech | (#50430-2-AP, rabbit polyclonal, RRID: AB_11042881 |
| Anti-γ-Tubulin | Proteintech | Clone 3F9H8, #66320-1-Ig, mouse monoclonal, RRID: AB_2857350 |
| Anti-Nesprin 3 | Abcam | #ab74261, rabbit polyclonal, RRID: AB_2243681 |
| Anti-Pericentrin | Abcam | #ab4448, rabbit polyclonal, RRID: AB_304461 |
| Goat anti-mouse/HRP conjugated secondary antibodies | Pierce/Thermo Fisher. | #PI-31430 |
| Goat anti-rabbit/HRP conjugated secondary antibodies | Pierce/Thermo Fisher. | #PI-31460 |
| Anti-goat HRP conjugated antibody | Invitrogen | |

| REAGENT or RESOURCE | SOURCE | IDENTIFIER |
|---|---|---|
| Alexa Fluor 488 goat anti-mouse IgG (H + L) | Life Technologies/Thermo Fisher scientific | (#A110010, Alexa Fluor 488 goat anti-Rabbit IgG (H + L) (#A11008) |
| Alexa Fluor 594 goat anti-mouse IgG (H + L) | Life Technologies/Thermo Fisher scientific | #A11032 |
| Alexa Fluor 594 goat anti-Rabbit IgG (H + L) | Life Technologies/Thermo Fisher scientific | #A11012 |
| Chemicals, peptides, and recombinant proteins | | |
| Cycloheximide (CHX) | Thermo Scientific | #357420010, Waltham, MA, USA |
| MG132 | Selleck Chemical LLC | #508339, Houston, TX, USA |
| Protein A plus G beads | Santa Cruz Biotechnology | #SC-2003 |
| Docetaxel | Thermo Scientific | #AC328420250 |
| Thymidine | Thermo Scientific | #AC22674 |
| Matrigel | Pierce/Thermo | #356230 |
| Trizol | Thermo Scientific | #15596026 |
| Crystal violet | Millipore/Sigma | #548-62-9 |
| Aprotinin | Millipore/Sigma | #A6106 |
| leupeptin | Millipore/Sigma | #L2884 |
| phenylmethylsulfonyl fluoride | Millipore/Sigma | PMSF, #P7626-1g |
| Cytochalasin D | BioTechne/Toris | #1233-1 |
| phospho-peptide CQDp**S**Gp**S**LHNp**S**SSGE/S1060/S1062/S1066/MYO10 | Thermo Fisher/Life Technologies Corp | N/A |
| non-phosphorylated peptide CQDSGSLHNSSSGE/S1060/S1062/S1066/MYO10 | Thermo Fisher/Life Technologies Corp | N/A |
| 4′,6-diamidino-2-phenylindole (DAPI) | Life Technologies/Thermo Fisher | #P36931 |
| Critical commercial assays | | |
| SYBR Green Master Mix | Invitrogen/Thermo Fisher Scientific | #FERK0362 |
| cDNA synthesis kit | Thermo Fisher Scientific | #K1622 |
| RNeasy Mini Kit | Qiagen, Crawley, UK | #74004 |
| cGAMP ELISA kit | Cayman Chemical | #501700 |
| BCA protein assay kit | Pierce/Thermo Scientific. | #23225 |
| Experimental models: Cell lines | | |
| Human osteosarcoma U2OS | ATCC | RRID: CVCL_0042 |
| Breast cancer MDA-MB-231 | ATCC | RRID: CVCL_0062 |
| Lung adenocarcinoma A549 | ATCC | RRID: CVCL_0023 |
| human embryonic kidney HEK293T | ATCC | RRID: CVCL_0063 |
| MYO10 knockout U2OS | Mayca Pozo et al.[27] | N/A |
| MYO10 knockout MDA-MB-231 | Mayca Pozo et al.[27] | N/A |
| GFP-MYO10 (wild type or mutants)/MDA-MB-231 | This paper | N/A |
| Experimental models: Organisms/strains | | |

| REAGENT or RESOURCE | SOURCE | IDENTIFIER |
|---|---|---|
| Athymic nude mice | Jackson Laboratory | #002019 |
| Oligonucleotides | | |
| See Table S1 | | N/A |
| Recombinant DNA | | |
| pEGFPC1-MYO10 | Mayca Pozo et al.[27] | N/A |
| pEGFPC1/F1-GFP-MYO10 (1–850 residues), | This paper | N/A |
| pEGFPC1/F2-GFP-MYO10 (810–1169 residues) | This paper | N/A |
| pEGFPC1/F3-GFP -MYO10 (1169–1510 residues | This paper | N/A |
| pEGFPC1/F4-GFP-MYO10 (1510–1698 residues), | This paper | N/A |
| pEGFPC1/F5-GFP-MYO10 (1698–2052 residues), | This paper | N/A |
| pEGFPC1/F2′-GFP-MYO10 (973–1169 residues) | This paper | N/A |
| pEGFPC1/-GFP -MYO10/S1060A | This paper | N/A |
| pEGFPC1/-GFP -MYO10/S1062R | This paper | N/A |
| pEGFPC1/-GFP -MYO10/L1063P | This paper | N/A |
| pEGFPC1/-GFP -MYO10/S1066A | This paper | N/A |
| pEGFPC1/-GFP -ΔDegron Deletion of residues from 1060 to 1066 | This paper | N/A |
| Flag-β-TrCP1 | Peschiaroli et al.[66] | N/A |
| Software and algorithms | | |
| GraphPad Prism software version 9.0 | GraphPad | GraphPad Software, CA, USA |
| ImageJ (Java-based image) | National Institutes of Health | https://ImageJ.nih.gov/ij/download.html |
| Mascot database | Matrix Science | Version 2.4, Matrix Science, London, UK |
| Other | | |
| DM6000B Leica fluorescence microscope with QImaging Retiga EXi CCD digital camera (Fast 1394 | Nuhsbaum Inc | N/A |
| Bio-Rad CFX96 Real-Time System | Bio-Rad Laboratories | N/A |
| Tanon 5200 Imager system | Tanon Inc | N/A |